Bachelor Thesis

K^0_S-p correlations in $\sqrt{S_{NN}} = 5.02$ TeV p-Pb collisions at ALICE

Remco de Boer
Student number: 3688364

Institute for Subatomic Physics
Utrecht University

Supervised by:
Prof. dr. Laura Fabbietti
Prof. dr. Raimond Snellings
Drs. You Zhou

15 January 2014

Abstract

This paper presents exploratory results from K^0_S-proton correlations in $\sqrt{S_{NN}} = 5.02$ TeV proton-lead collisions at ALICE. To obtain high K^0_S purity and yields, cuts on pion V0 pairs have been analyzed. An analysis on proton purity as a function of p_T with different nSigma cuts has also been performed. These purities have been used as weights in correlating K^0_S with protons. The resulting correlation functions show a strong correlation effect that is probably due to 'particle mini-jets'. A comparison with K^0_S-K^+ correlation in the same data set confirms that the effect is not due to K^0_S-p correlation in the particle emitting region. Together with a summary of the findings of this study, suggestions for further research to reduce this 'mini-jet' background are also presented.

Contents

1 Introduction

The Large Hadron Collider (LHC) of CERN in Geneva, Switserland, is currently the largest particle accelerator in the world and it can collide particles at unprecedented high energies. Collisions (or *events*) occur about 600 million times per second[1] emitting millions of particles that are detected in the LHC detectors. The bulk of these particles are soft hadrons which decouple from the collision region in the late hadronic freeze-out stage of the event evolution. The characteristics of these particle ensembles carry information about the early stages of the collision. This information reveals the properties of matter at these high energy densities – energy densities that existed just after the big bang – and can thus give insight to the origin of the universe.[1]

The main detectors at the LHC are ATLAS and CMS (generally designed to verify the existence of the Higgs boson), LHCb (designed to study the asymmetry between matter and antimatter), and ALICE which is the detector that has been used in this study. It is designed to study Quark Gluon Plasma (QGP), a de-confined state of matter that is predicted by Lattice Quantum Chromo-Dynamics (QCD).

QGP is not yet fully understood and many of its properties are still being studied. This study focuses on determining the space-time extent of the particle emitting region, the QGP state. It can be determined by analyzing two-particle momentum correlations which are sensitive to the space-time separation of the particle emitters.[2] This effect is due to quantum statistics and final-state interactions that introduce interference in amplitudes.[4] For this reason the measurement of particle correlation is called *interferometry*.[3]

Of particular interest in this study is the correlation between K^0_S and protons. As opposed to for instance pion-pion pairs (which give large yields), K^0_S-p pairs are not influenced by final-state Coulomb interaction. Furthermore the reconstruction method of K^0_S (an unobservable neutral particle) makes it possible to obtain high K^0_S purity even at high momenta, whereas pion identification starts to fail around 4 GeV/c. Furthermore, the fact that K^0_S is reconstructed means that correlating protons to K^0_S does not result in *track merging*. Not much research has been done on this type of correlation, since the scattering length of p-K^0_S interaction is too small to give rise to a distinguishable correlation.[12] At higher energies, such as those produced in the LHC, different effects could arise, especially in asymmetric p-Pb collisions. With the new p-Pb collision data from ALICE, this project had to start from scratch and its results should thus be viewed as exploratory work in these types of collisions.

2 Experimental setup

Particles are characterized by their mass and charge. Mass however, cannot be directly determined, so particles need to be distinguished by means of quantities that can be measured: momentum, velocity, and energy. These quantities are measured by determining the tracks of emitted particles. Tracks are determined using the ITS, TPC, and TOF detectors of ALICE, which are discussed in the next section. These observed tracks are curved due to strong magnetic and electric fields in the detectors and thus give us information about the particle that produced these tracks.

The full information about track and collision vertex data (ESDs) consists of an incredible amount of data points. For this reason smaller data files (Analysis Object Data, AOD) are constructed using the track data combined with information about the fields in the detector. These AODs are small enough in file size to be analyzed offline, because they only contain reconstructed one-dimensional data members like collision centrality, coordinates of the position where the collision took place (the *primary vertex*), distance of closest approach to the primary vertex, momentum at the moment of closest approach, average energy loss, and time-of-flight.

AOD containing several p-Pb collision runs has been analyzed offline for this study. The AOD not only contained track information, but also pairs of pion tracks identified using the TPC and TOF detectors, that were used to find K^0_S. The track information was used to identify protons, and later kaons as well, for the correlation comparison.

[1] This is in the case of proton-proton (p-p) collisions. Lead-lead (Pb-Pb) collisions are also studied, as are asymmetric ion collisions (like p-Pb) which are of particular interest in this thesis.

2.1 The ALICE detectors

ALICE (A Large Ion Collider Experiment), as its name suggests, is designed to study heavy ion collisions.[2] The energies of collisions at the LHC are so high that collided particles become Lorentz-contracted, that is, in the laboratory frame they have the shape of a disc in the plane transverse to the beam. The result is that particles emitted at a collision event are emitted in a direction close to the transverse plane. Particle momenta $\vec{p}$ are therefore expressed in a coordinate system $p_x\hat{p}_x + p_y\hat{p}_y + p_z\hat{p}_z$ where the orthonormal vectors $\hat{p}_x$ and $\hat{p}_y$ lie in the transverse plane and $\hat{p}_z$ is chosen in the direction of the accelerated protons in the beam. In high-energy collisions, more convenient quantities are often used: the *transverse momentum* $p_{\mathrm{T}} = \sqrt{p_x^2 + p_y^2}$ and *pseudorapidity* η, which is a measure for p_z and is given by

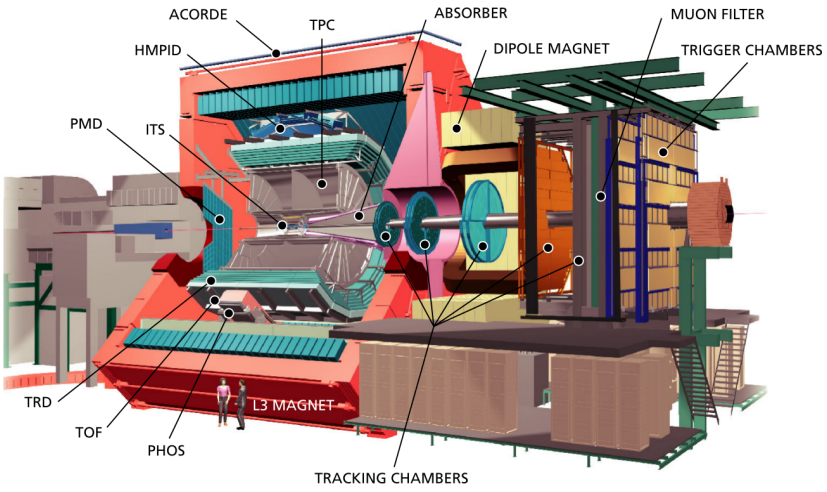

Figure 1: ALICE and her detectors presented schematically.[1]

$$\eta = \tfrac{1}{2}\log\left(\frac{|\vec{p}| + p_z}{|\vec{p}| - p_z}\right). \tag{1}$$

Another useful (particle specific) measure is that of *rapidity* y which has the same definition as η except that the energy E is used instead of momentum length $p = |\vec{p}|$.[3] A third coordinate ϕ gives the *azimuthal angle* in the transverse plane, but this coordinate is not used in this study.

ALICE has several detectors which are shown in Figure 1. The most important ones, the TPC, the TOF detector, and the ITS, are located cylindrically in the transverse plane around the point of interaction. These detectors can determine tracks accurately in the range $|\eta| < 0.9$. Outside this range, particles can only be tracked over a shorter radius, so often (as in the data set used) rapidity is cut up to $|\eta| < 0.9$. The detectors cover 360° of the azimuth, but it should be noted that due to the construction of ALICE the sensitivity over this range is not uniform.

In the next four subsections, the functionality and resolution of the detectors that were used for this study are explained.

2.1.1 Inner Tracking System (ITS)

The ITS is the smallest of the track detectors and is located immediately around the beam. It is also the finest detector as the track density is largest here. It consists of four Silicon Pixel Detector (SPD) layers and two Silicon Drift Detector (SDD) layers that can measure particle locations with a resolution better than 100 μm. Its inner radius is 3 cm, being also the smallest radius where particles can be tracked, and its outer radius is 44 cm, which is where the TPC starts. The ITS is mostly used to determine centrality and energy loss (which is used for particle identification). The ITS measures particles in the range $0.1 < p_{\mathrm{T}} < 3$ GeV/c and is therefore used as a complement to the Time Projection Chamber.

2.1.2 Time Projection Chamber (TPC)

Around the ITS is the cylindrical Time Projection Chamber. It is the main tracking device of ALICE since it covers a large range where particles can be accurately tracked over a long range. Its inner radius

[2] This section is based on several dissertations of the ALICE group, but the facts were found in source [1].

[3] In relativity, the 'rapidity' β is defined as $\beta = v/c$, but in this paper we refer to this quantity as *relativistic rapidity*.

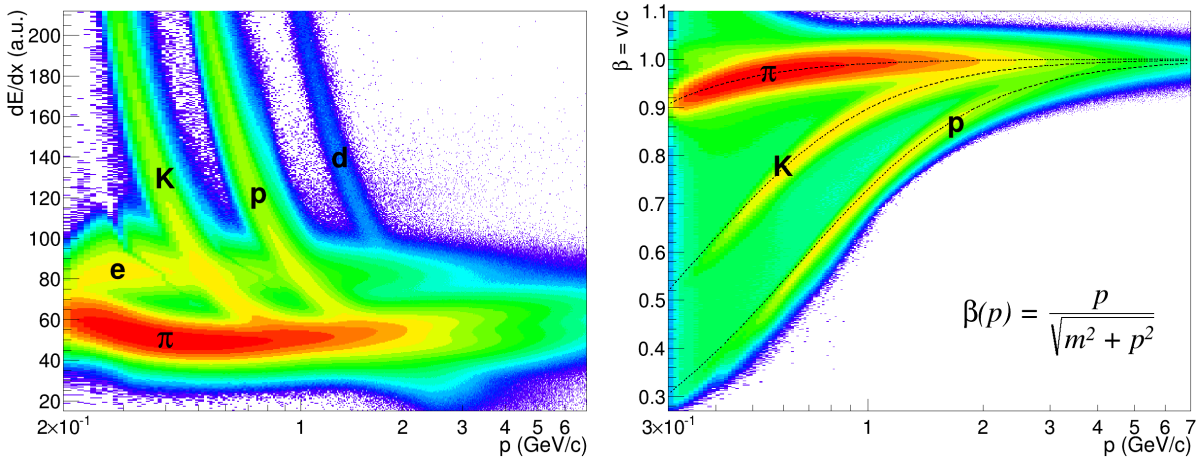

(a) Energy loss $\frac{dE}{dx}$ versus momentum p as a PID using the TPC detector.

(b) Relativistic rapidity β versus momentum p as a PID using the TOF detector.

Figure 2: Two relations that help to identify particles in ALICE.

is 80 cm, its outer radius 250 cm, and its length is 5 m. It contains a gas mixture that ionizes locally when an emitted particle passes. A highly uniform electric field of about 400 V/cm that is parallel to the beam accelerates the ejected electrons towards either cathode at the side cap of the detector. A wire frame here collects the electrons and provides radial information about the tracks that the particles create in the gas mixture. The time it takes the ejected electrons to move to the cathode (the *drift time*) provides the z-component of the track data points. The curvature of the tracks gives information about the initial momentum of the particle. The TPC can measure particles in the range $0.1 < p_{\mathrm{T}} < 100$ GeV/c with a transverse momentum resolution of less than 6%,[4] and even more accurate up to 20 GeV/c, namely 4.5%. From around 60 GeV/c the resolution is about 25%.

Particle identification can also be done using combined information from the TPC and the ITS. The density of the collected electrons gives an indication of the energy loss $\frac{dE}{dx}$ of the emitted particle. The energy loss depends on many variables, but most importantly on charge, mass, and momentum p. The relation between $\frac{dE}{dx}$ and p is complicated, but is described by the Bethe-Bloch equation. In Figure 2a the relation can be clearly seen: $\frac{dE}{dx}$ dependence on mass and charge results in distinguishable bands that are due to the difference in particles mass. A general trend is that heavier particles such as protons (p) and deuterium (d) lose energy at a higher rate, however at higher p (starting from about 0.8 GeV/c) the bands start to overlap and particle identification becomes less reliable.

Taking p-slices[5] of this $\frac{dE}{dx}$ versus p distributions results in sums of Gaussians. The Gaussians correspond to particles. Their centre is determined by the Bethe-Bloch equation and their width σ depends on the resolution and accuracy of the detector. For PID in the AOD files a special PID measure *nSigma* has been defined. When a track has momentum p, *nSigmaTPC* is defined as the difference between $\frac{dE}{dx}(p)$ of measured track and $\frac{dE}{dx}(p)$ of the hypothesized particle, divided by the width σ at p. This measure can be used as a PID. For instance, an '2SigmaPiTPC cut' means that only tracks that have nSigmaTPC < 2 in the pion hypothesis are selected.

2.1.3 Time-Of-Flight detector (TOF)

The TOF is a cylindrical surface around the TPC. It is primarily used as a second particle identification. It is 7.5 m in length and has a radius of 4 m. Resistive plate chambers filled with gas that is ionized once a particle passes can determine the time between the moment of collision and the moment of arrival in the TOF. Its accuracy is about 100 ps.

[4] It is 6% in Pb-Pb collisions, which involve thousands of tracks – a factor 10^3 more than in p-Pb collisions.
[5] Often, as in this study, p_{T}-slices are used.

The time-of-flight together with the track length (determined using the TPC and the ITS) can be used to determine the average velocity and thus the relativistic rapidity β. The relation between momentum p and β is given by

$$\beta(p) = \frac{p}{\sqrt{m^2 + p^2}}, \tag{2}$$

and depends on the mass m of the particle. This relation can be seen in Figure 2b. Again, distinguishable bands can be seen, however, the TOF bands can be distinguished at even higher p (up to about 4 GeV/c) to identify particles than the $\frac{dE}{dx}$ bands of the TPC. The width σ of the band depends in a complicated manner on the uncertainty in for instance the track length, the moment of the collision (*trigger time resolution*), and the time resolution of the TOF. This is used to define a PID measure in a way similar to that of nSigmaTPC. Cuts on the β distribution are therefore called *nSigmaTOF cuts*.

2.1.4 The VZERO detector

Many of the particle characteristics discussed above depend on the location of the primary vertex and on the centrality (see Section 2.2) of the collision. This is determined mainly by the VZERO detector, which is located at the side caps of the ITS. It consists of two detectors: VZEROA which is located 340 cm from the point of interaction and VZEROC which is located 90 cm from the point of interaction. The VZERO detectors measure remnants of the collision with high pseudorapidity. They provide a two-dimensional distribution of these remnants which is used to determine the position of the primary vertex. Centrality depends on the number of particle (the *multiplicity*) and can also be determined with the VZERO detectors.[6]

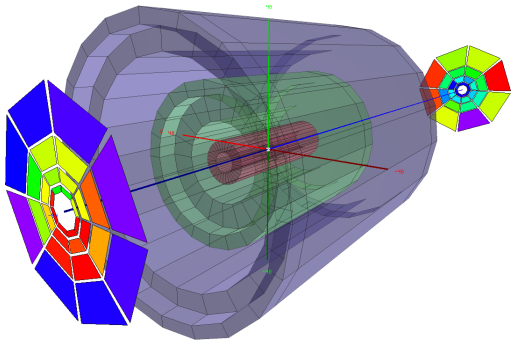

Figure 3: VZEROA (back) and VZEROC (front) alongside the ITS (middle).

2.2 Proton-lead collisions and multiplicity

The LHC was designed to collide protons and to collide lead ions (Pb). These p-p collisions (7 TeV) and Pb-Pb collisions (2.76 TeV) result in completely different physical situations. p-p Collisions emit only a small number of particles (in the order of 10) and are collisions between point-like protons with extremely high energy densities, while Pb-Pb collisions emit a much larger number of particles (in the order of ten thousand) and are collisions between a mixture of nucleons. Other *symmetric* collisions like Au-Au (gold-gold) have also been performed.

An important measurement in these symmetric collisions is the degree of overlap between the two colliding particle cores. In p-p collisions this is often given by the *impact parameter*, the distance between the two proton cores. In Pb-Pb collisions the impact parameter can also be defined, but the degree of overlap is usually expressed in terms of *centrality*, a quantity measured in percentages ranging from 0 to 100%. However, since the impact parameter is in the order of sub-atomic scales, it cannot be determined exactly, but the multiplicity, which *can* be measured, depends on the degree of overlap (a large overlap results in high multiplicities of emitted particles) and can therefore be used as a measure for centrality (which has a less accurate definition than the impact parameter). Furthermore, p-p and Pb-Pb can be simulated with Monte Carlo (MC) simulations employing the Glauber model, which do have a known impact parameter. MC simulations can be used to find the relation between multiplicity and centrality or impact parameter. Therefore centrality is a well defined notion in p-p and Pb-Pb collisions.

Since 21 January 2013 asymmetric p-Pb collisions have been performed at the LHC as well.[7] Proton-lead collisions are asymmetric collisions and therefore show a different behaviour than symmetric collisions.[8] More problematic though is the determination of centrality. One could say that the impact parameter

[6] Source of Figure 3: `http://aliceinfo.cern.ch/Public/en/Chapter1/Events-en.html`

[7] `http://home.web.cern.ch/about/updates/2013/01/protons-smash-lead-ions-first-lhc-collisions-2013`

[8] See for example source [6] for an effect that depends on centrality in p-Pb data.

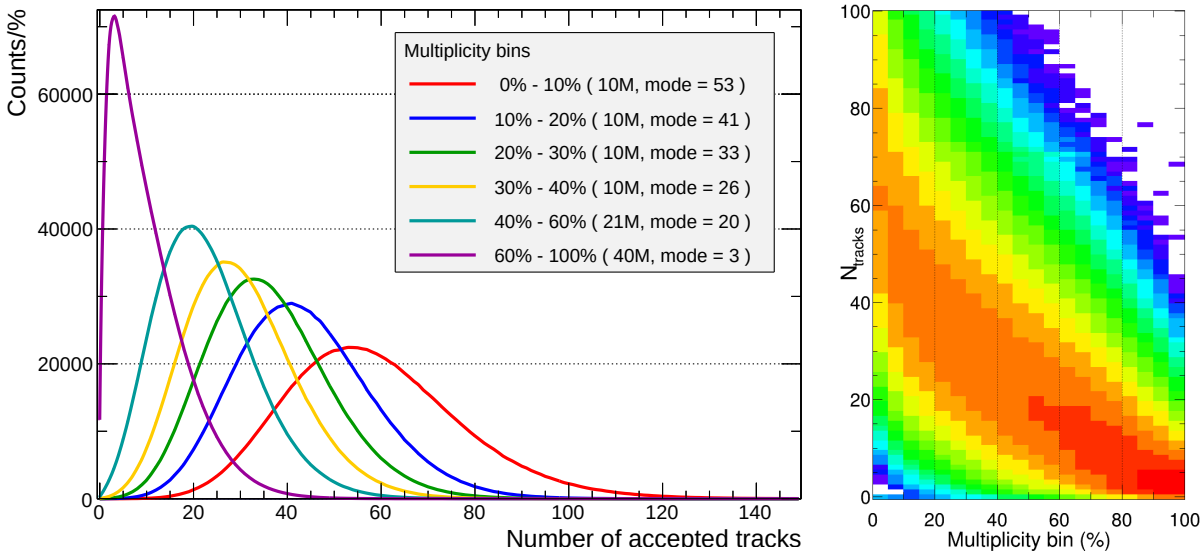

(a) (b)

Figure 4: Multiplicity distribution per multiplicity bin (a) and number of tracks distribution versus multiplicity bin (b).

in p-Pb collisions is well determined, but the relation between centrality and multiplicity determined by the Glauber model applied on p-Pb collision is different than that found in p-Pb collision data. Research is still being done to correct this mismatch, so at the moment a more rough definition of centrality is used in p-Pb collisions. To avoid confusion, the term *multiplicity bin* has been introduced, as events are often categorized in a small number of wide 'centrality' bins.

In this study, events have been categorized into six multiplicity bins: 0-10%, 10-20%, 20-30%, 3-40%, 40-60%, and 60-100%. In this definition, 0% means a 'frontal' collision. Collisions in this bin have the largest multiplicity. The multiplicity distributions for different multiplicity bins can be seen in Figure 4a. The number of entries has been divided by the width of the multiplicity bin. The general relation between the multiplicity (N_{tracks}) and the multiplicity bin is shown in Figure 4b with a finer binning.

2.3 Data set

This analysis has been performed on pPb data from ALICE AOD139. The 23 runs studied were

> 195334, 195351, 195389, 195391, 195479, 195480, 195481, 195482, 195483, 195529, 195531, 195566, 195567, 195568, 195592, 195593, 195596, 195633, 195635, 195644, 195673, 195675, 195677.

These runs together comprise a total of **102 million** p-Pb collisions at a centre-of-mass energy of $\sqrt{S_{NN}} = 5.02$ TeV.
The analysis was done using the ROOT version 5.34/10 (29 August 2013). If there is no specific explanation on error bars, the error bars have been defined by the standard statistical definition in ROOT, that is, the error in bin i is given by $1/\sqrt{S_i}$ where S_i is the number of entries in bin i. Errors of fit parameters have also been computed using the standard ROOT functions and are variational fit errors. If no source for a specific histogram in this paper has been mentioned, it was produced using this data set.

2.4 Particles that were studied

Charged particles that are of interest to this study are protons (p), positive pions (π^+), and negative pions (π^-). The pions were used to reconstruct K^0_S. *Phases space distributions* (momentum p versus rapidity y) for each of these particles are shown in Figure 5. Only tracks in the range $|\eta| < 0.8$ were selected. These figures show that the particles do not have a uniform (pseudo)rapidity distribution, which

is mostly due to black spots in the detector, but in this study no rapidity binning is used, so no correction has been applied to it. Positive kaons (K^+) have also been in this study, but the phase space distribution of the kaons is not much different than that of the protons and is therefore not shown.

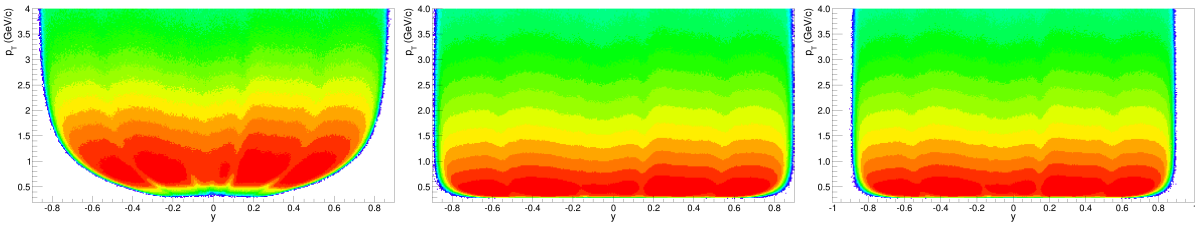

(a) Proton (p) (b) Negative pion (π^-) (c) Positive pion (π^+)

Figure 5: Phase spaces for the three particles we can detect. Note that there is a cut $p_{\mathrm{T}} > 0.2$ GeV/c.

K^0_S is a *weak eigenstate* of the weak force. Its quark content is a linear combination of down (d) and strange (s) quarks, $\left(d\bar{s} - s\bar{d}\right)/\sqrt{2}$. These two quark combinations are the neutral kaon and its anti-particle.[9] The eigenstates are however not exact due to *CP violation*. The K^0_S mass is 497.614±0.024 MeV. As noted before, the K^0_S decay mode that is studied here is $K^0_S \rightarrow \pi^- + \pi^+$. Pions are also mesons, consisting of two valence quarks: $\pi^- = \bar{u}d$ and $\pi^+ = u\bar{d}$. Their mass is 139.57018 ± 0.00035 MeV. The proton is a hadron and is composed of three valence quarks: two up-quarks and one down-quark (uud). Its mass is 938.272046 ± 0.000021 MeV.[10]

3 Analysis methods

This research project consisted of three parts.

1. Reconstructing K^0_S and finding the optimal cuts on the pion V0 pairs.
2. Computing the proton purity as a function of transverse momentum.
3. Extracting the K^0_S-p correlation.

The followed procedures will be explained in chronological order. The used cut values and results are omitted here and are presented in Section 4.

3.1 K^0_S reconstruction

K^0_S particles have to be reconstructed from their decay into charged particles. The predominant decay mode of K^0_S is $K^0_S \rightarrow \pi^+ + \pi^-$ with a branching ratio of $69.20 \pm 0.05\%$. Other modes either involve only neutral particles or have a negligible probability of occurring.[7] These opposite charged pion pairs will be referred to as *V0 pairs*.

Given a V0 pair, the two pions are assumed to stem from a K^0_S decay. The location of the decay is referred to as the *secondary vertex*. It is assumed that this secondary vertex lies at the midway of the positions where the pions were observed for the first time. The topological situation is graphically presented in Figure 6. Only the thick blue and red tracks and the location of the event (the *primary vertex*) can be directly determined. The pions can however be uncorrelated, so other parameters need to be found that can be cut in order to increase the probability that the pions were produced in a K^0_S decay. These parameter cuts will be used as particle identification (PID) for K^0_S when correlating protons and K^0_S.

3.1.1 V0 parameters

Four variables will be used to identify K^0_S. They are graphically presented in Figure 6.

[9] The strong eigenstate is K^0_L ("K^0-long") and is given by $\left(d\bar{s} + s\bar{d}\right)/\sqrt{2}$.

[10] See *Particle Data Group*, e.g. source [7].

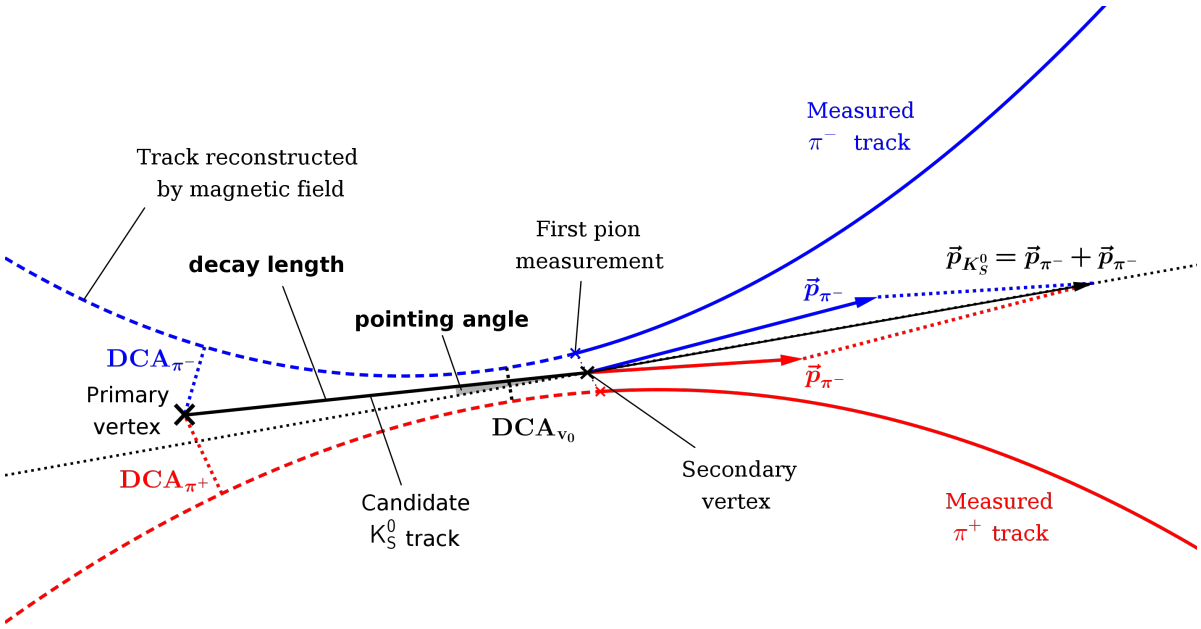

Figure 6: Topology of the K^0_S decay. The coloured tracks correspond to tracks of charged particles which can be measured and used to compute their characteristic parameters.

1. **Decay length** ($c\tau$) is defined as the distance between the primary vertex and the secondary vertex. Since K^0_S has a decay length of about $c\tau \approx 2.69$ cm, only values below a certain **maximum** are selected.

2. **Pointing angle** ($\cos\alpha$) is defined as the angle between the K^0_S track and the momentum $\vec{p}_{K^0_S}$ of the reconstructed K^0_S. For convenience, the *cosine of the pointing angle* will be used. It is 1 in the ideal case. A **minimal** value cut will be applied to this variable.

3. **Distance of closest approach of the V0 ($DCA_{K^0_S}$)** is the minimal distance between the two tracks of the pions. This distance is 0 in the ideal case, so a **maximal** value cut will be applied.

4. **Distance of closest approach of the pions ($DCA_{\pi^\pm}$)** is the minimal distance between the primary vertex and the track of the pion (in both the backward computed and the measured range of the track). A **minimal** value cut will be applied to this variable in order to select pion pairs that separate geometrically after the moment of K^0_S decay.

These four variables proved to be sufficient to obtain a reasonable purity (see Section 4.1).

3.1.2 K^0_S yield and purity

Cuts on the variables discussed in Section 3.1.1 need to be optimized in order to obtain a suitable purity and a sufficient yield for the correlation. The K^0_S purity and K^0_S yield is estimated using the invariant mass distribution $N(m)$ of the V0 in a large number events. The invariant mass can be computed with

$$\begin{aligned} m_{K^0_S}(\vec{p}_{\pi^-}, \vec{p}_{\pi^+}) &= \sqrt{(E_{\pi^-} + E_{\pi^+})^2 - |\vec{p}_{\pi^-} + \vec{p}_{\pi^+}|^2} \quad = \\ &= \sqrt{2\sqrt{m_\pi^4 + m_\pi^2\left(p_{\pi^-}^2 + p_{\pi^+}^2\right)^2 + p_{\pi^-}^2 p_{\pi^+}^2} - \vec{p}_{\pi^-} \cdot \vec{p}_{\pi^+}} \end{aligned} \tag{3}$$

where $\vec{p}_{\pi^\pm}$ is the pion momentum. The momentum of the K^0_S at the moment of decay is

$$\vec{p}_{K^0_S} = \vec{p}_{\pi^-} + \vec{p}_{\pi^+}. \tag{4}$$

Uncorrelated V0 pairs contribute to a non-Gaussian background distribution, correlated pairs contribute to a signal peak distribution centred around[8]

$$m_{\mathrm{K}^0_{\mathrm{S}}} = 497.614 \pm 0.022 \text{ MeV} \tag{5}$$

in the invariant mass distribution. The background distribution has been fitted with a polynomial function $N_{\mathrm{bkg}}(m)$ of degree 2 and the signal with a Gaussian function

$$N_{\mathrm{sig}}(m) = N_0 \exp\left(-\frac{(m-m_0)^2}{2\sigma^2}\right). \tag{6}$$

with non-fixed parameters m_0, N_0, and σ. The yield is then defined as Sig and the purity as Sig/(Bkg+Sig) where

$$\text{Sig} := \int_{m_0-3\sigma}^{m_0+3\sigma} N_{\mathrm{sig}}(m)dm \qquad \text{Bkg} := \int_{m_0-3\sigma}^{m_0+3\sigma} N_{\mathrm{bkg}}(m)dm. \tag{7}$$

The error in the purity is defined as purity$/\sqrt{\text{Sig}+\text{Bkg}}$. Note that a 3σ-range has been used in the integral.

Tight cuts result in high purity but low yields, so a balance between the two needs to be found. Different cut combination have been defined and numbered by *cut indices*, which can be used to plot the purity and the yield for several cuts in order to find an optimal cut combination for a balanced purity and yield. The purity of the $\mathrm{K}^0_{\mathrm{S}}$ candidates is found to be around 0.98, so the $\mathrm{K}^0_{\mathrm{S}}$ purity will not be used as a weight in the correlation.

3.2 Proton purity as a function of p_{T}

Protons are identified using the TOF and TPC detectors (see Section 2.1). At high p_{T}, the proton identification gives a large background. For this reason the proton purity and proton yield have been analyzed as a function of p_{T}. The extracted purities are then used as a weight for the protons in the $\mathrm{K}^0_{\mathrm{S}}$-p correlation. The proton purity has been computed for different nSigmaTOF cuts using the nSigmaTPC distribution in the proton hypothesis.[11] If not mentioned specifically, nSigma refers to nSigma in the proton hypothesis (also denoted as nSigma**P**TPC).

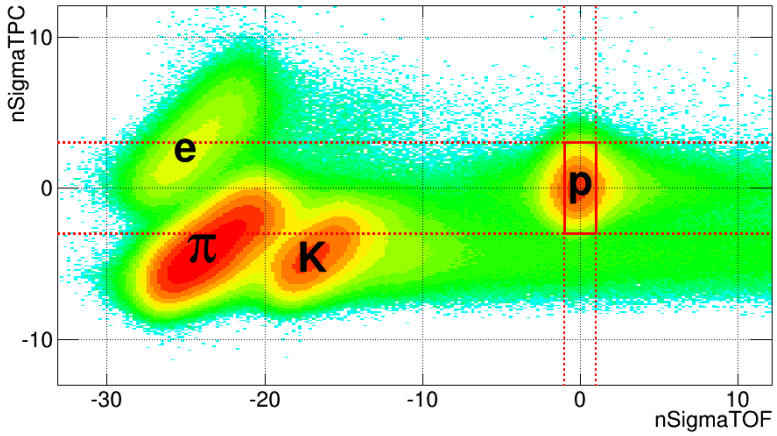

Figure 7: nSigmaTPC versus nSigmaTOF in the range $1 < p_{\mathrm{T}} < 1.125$ GeV/c. In this range particles can still be distinguished. The red lines show the cuts that were used in the $\mathrm{K}^0_{\mathrm{S}}$-p correlation.

The nSigmaTPC versus the nSigmaTOF distribution in different p_{T} bins, shows us at which p_{T} bin a negligible background is expected. Figure 7 shows this distribution in a p_{T} bin where the electrons (e), pions (π), kaons (K) and protons (p) can be distinguished well. The red lines show the cuts that were

[11] See Section 2.1 for the definition of nSigmaTOF and nSigmaTPC in a p_{T} bin.

used in the K^0_S-p correlation (|nSigmaTPC| < 3 and |nSigmaTOF| < 1). In Figure 8, left panel, the TPC cut can reject pions and kaons, but in most p_T bins, the TPC cut cannot separate protons from other particles. In Figure 8 on the right panel, the reverse is true: the TPC cut is sufficient for the kaon rejection since in this p_T range the pion and kaon 'cloud' move up. The combination of TPC and TOF cuts can give high proton purities up to p_T around 3.5 GeV/c.

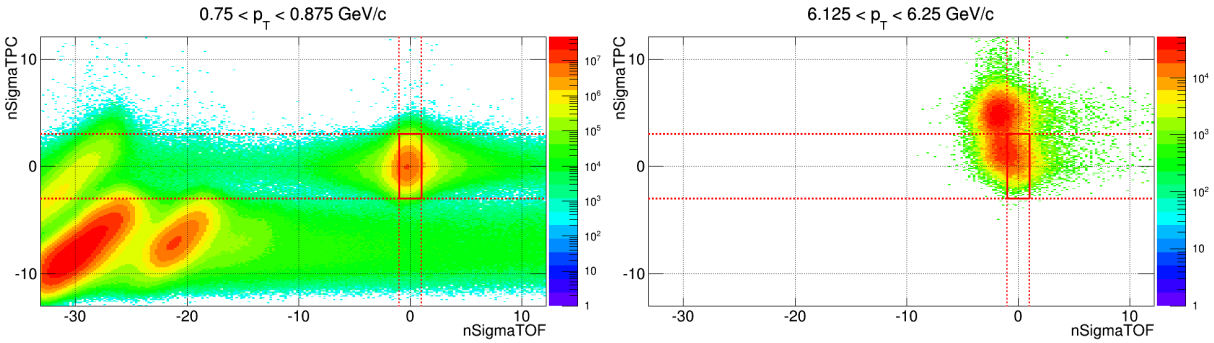

Figure 8: nSigmaTPC versus nSigmaTOF in low and high p_T bins. The distributions include all tracks, also low-cluster and high χ_{TPC} tracks, and therefore show distortions.

Projecting these distributions down to the nSigmaTPC axis for different p_T bins gives us a distribution than can be fitted with the sum of four Gaussians (one for each particle species: protons, pions, kaons, and electrons, their associated anti-particle included). One of the Gaussians is centered around 0 and has width 1 in units of nSigmaTPC. This represents the contribution of the protons. The integral over this distribution in a certain nSigmaTPC range (±3SigmaTPC was used in this study) divided by the integral over the other three Gaussians gives us the *proton purity*.
It is however hard to fit the nSigmaTPC distribution at high p_T where the Gaussians are hard to distinguish. Therefore a 'distribution fit method' was applied that consisted of extracting four nSigmaTPC distributions (from here on addressed as *particle distributions*) on which a tight TOF cut (0.5σ to have high purity) had been applied in their respective particle hypotheses. These experimental distributions for different particle species are nearly Gaussian distributions centered around the position on the total nSigmaTPC distribution where the associated particle should be. In each p_T bin, a linear combination of these four particle distributions was fitted to the nSigmaTPC distribution. The yield is then defined as the integral over the proton distribution and the purity as the yield divided by the integral over the other three particle distribution on the range $[-3\sigma, 3\sigma]$ in the proton hypothesis.

3.3 K^0_S-p correlation

After having found the optimal cuts on the V0 pairs and the proton purity as a function of p_T, the K^0_S can be correlated with the protons. There are several ways of defining a correlation function $C(\vec{p}_1, \vec{p}_2)$ which is a function of the momenta $\vec{p}_1$ and $\vec{p}_2$ of the two particles.[10] Usually it is defined in terms of the *relative momentum* $\vec{q}$ between the two particles (see Figure 9 for a geometrical representation). This gives a three-dimensional function which requires fine binning (and thus large statistics) to be determined.

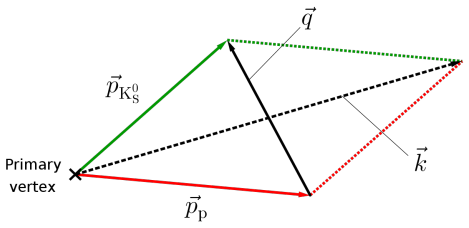

Figure 9: Relative momentum $\vec{q}$ and sum of the momenta $\vec{k}$.

Therefore in this study, as in most other studies, a one-dimensional projection of $\vec{q}$ is used. In this paper three variables have been used: the length q_T of the relative momentum projected to the transverse plane, the length q of the relative momentum and the invariant relative momentum q_{inv}, which is defined as

$$q_{inv} := \sqrt{q^2 + q_0^2} = \sqrt{q^2 + (E_2 - E_1)^2} \tag{8}$$

where E_1 and E_2 are the energies of the particles, given by $E = \sqrt{m^2 + p^2}$. The correlation functions in

this paper are thus one-dimensional and are easier to analyze.

The correlation function is a theoretical construct, but it is in fact simply a way of comparing a correlated with an uncorrelated set of particles. When particles are correlated, they move in the same direction and their relative momentum is close to 0. Constructing the correlation function thus comes down to comparing a *foreground distribution* of the variable of interest in a correlated situation to a *background distribution* in an uncorrelated situation. The construction of the foreground and background distributions will be discussed first and the correlation functions will be defined in terms of these two distributions.

3.3.1 Same event distribution

Each event contains a number of pion V0 pairs and a number of tracks. Given an event trigger, a loop runs over all V0 pairs and stores them when they fulfill the optimal K^0_S cuts. This gives a total number $N_{\mathrm{K}^0_\mathrm{S}}$ of K^0_S in this event. In the same event a loop runs over all tracks and stores them when they fall within the TOF and TPC cut. To remove autocorrelations, tracks are not stored if they have the same track ID as any of the pions of the selected V0 pairs. This gives us N_p protons. The N_p purities corresponding to the p_T bin in which a proton falls is also stored.
A third double loop then runs over all $N_{\mathrm{K}^0_\mathrm{S}} \times N_p$ stored K^0_S and protons and computes their q, q_T, and q_inv. These variables are filled in a distribution using the weight corresponding to the correlated proton. The multiplicity bin of each event is also stored. The resulting distribution is taken as the foreground distribution.

3.3.2 Event mixing

The foreground distribution needs to be compared to an uncorrelated distribution. This can be obtained by using the same procedure as above, but this time correlating K^0_S from the base event to protons from other events. A loop runs over the next N_p events that fall in the same multiplicity bin and stores the first track that falls within the TOF and TPC cuts.[12] In the third loop these protons are then correlated with the K^0_S in the base event with their corresponding purity weights. The resulting distribution is the (combinatorial) background distribution. It has exactly the same number of entries (N) as the foreground distribution.[13] Note that in both procedures none of the pairs are stored more than once.

3.3.3 Correlation function

In this paper two correlation functions will be studied: a ratio function $C_\mathrm{rat}(q)$ and a difference function $C_\mathrm{dif}(q)$. The difference function gives an indication of the discrepancy between the foreground and the background distribution. The ratio function is used for the determination of the space-time extend of the particle emitting region. The two correlation functions are defined by

$$C_\mathrm{rat}(K) := \frac{\mathrm{foreground}(K)}{\mathrm{background(K)}} \qquad C_\mathrm{dif}(K) := \frac{\mathrm{foreground}(K) - \mathrm{background(K)}}{N}. \tag{9}$$

where K can be q, q_T, or q_inv and N is the total number of entries. This means that the content of each bin in the foreground distribution is divided, resp. subtracted, by the corresponding bin in the background distribution. If there is no correlation at all $C_\mathrm{rat}(K)$ should be 1 everywhere and $C_\mathrm{dif}(K)$ should be 0.

[12] In the unfortunate case where there are not N_p consecutive events in the same multiplicity bin, the loop is aborted and the base event is skipped.

[13] The usual procedure is to pick a constant number of protons from the next event(s). This does not result in the same amount of entries as in the foreground distribution, so both distributions are then normalized to unity. The procedure described above is not necessary, but results in an equal amount of statistics.

4 Results

4.1 Optimization of the K^0_S cuts

A systematic comparison between combinations of the different V0 pair cuts has been performed in order to maximize the total K^0_S signal and the purity simultaneously. For each cut combination, the resulting invariant mass distribution of the candidate K^0_S (like the one in Figure 10) was used to compute the yield and purity as defined in Section 3.1.2. Based on the distributions of the four cut variables defined in Section 3.1.2, a number of minimal and maximal cuts have been defined on decay length (**Decl** for short), the cosine of the pointing angle (**Angl**), the minimal DCA of *both* pions (**DCAp**), and the DCA of the V0 pair (**DCAv**). See Table 1.

Cut index	**Decl** max (<)	**Angl** min (>)	**DCAv** max (<)	**DCAp** min (>)
0	no cut	no cut	no cut	no cut
1	100 cm	0.998	1.0 cm	0.5 cm
2	80 cm	0.9995	0.5 cm	1.0 cm
3	60 cm	0.9999	0.3 cm	2.0 cm
4	50 cm		0.1 cm	3.0 cm
5	30 cm			
×	10^3	10^2	10^1	10^0

Table 1: Definition of the cut indices

These cuts were numbered with digits starting from 0 (being no cut at all). Combinations (i.e. sums of the digits multiplied by a power) of these digits have been used as cut definitions. For each of the 600 combinations, or *cut indices*, the K^0_S purity and yield has been computed. The result for each of these cut indices is shown in Figure 11. In this figure the cuts that lead to a purity larger than 0.97 and a yield larger than 3.5×10^7 are marked in green. The optimal cut is found to be **cut index 5241** with:

decay length cuts	Decl	$<$	30 cm,
cos. pointing angle	Angl	$>$	0.9995,
DCA between pions	DCAp	$<$	0.1 cm,
individual pion DCA	DCAv	$>$	0.5 cm,

Using these cuts a K^0_S yield of 3.80×10^7 and a K^0_S purity of $\mathbf{0.976 \pm 0.005}$ is obtained.

A further check on the K^0_S signal could be the extraction of the decay length of the K^0_S candidates. This however has to be computed with efficiency corrected data, so it has not been done in this study.

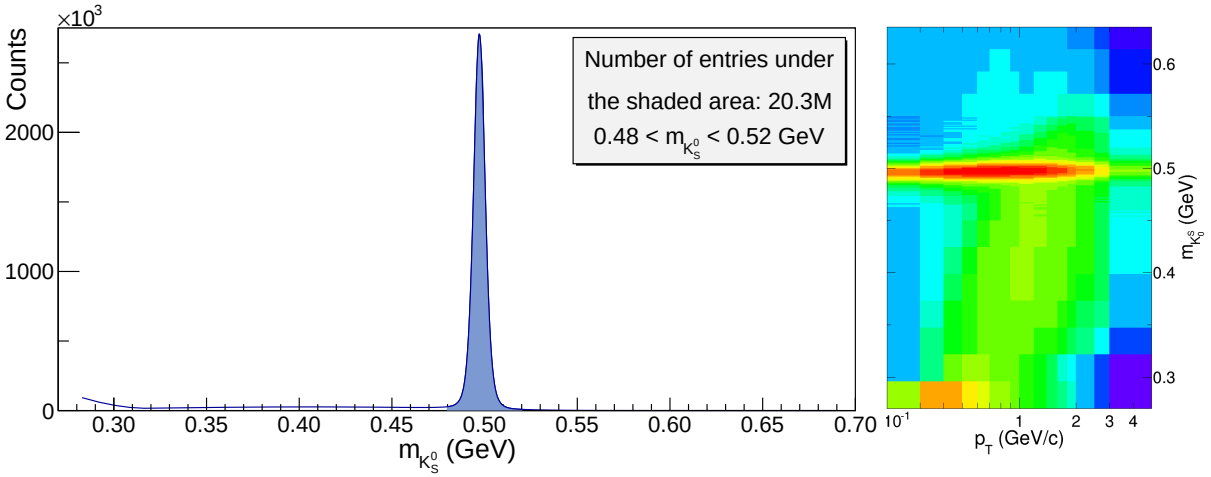

Figure 10: Invariant mass distribution of the candidate K^0_S with the optimal cut. On the right panel the nature of the background can be seen in the $m_{K^0_S}$ versus p_T logarithmic distribution.

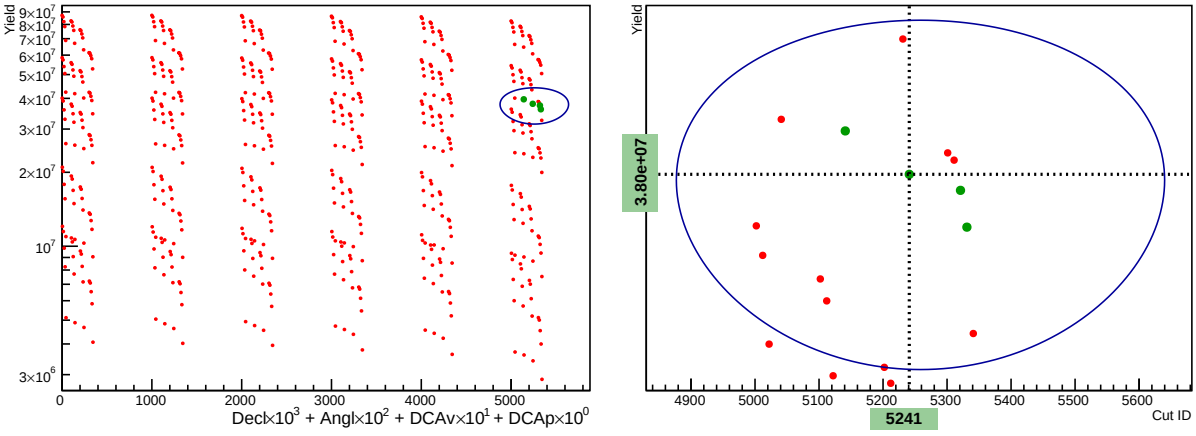

(a) K^0_S yields versus cut index

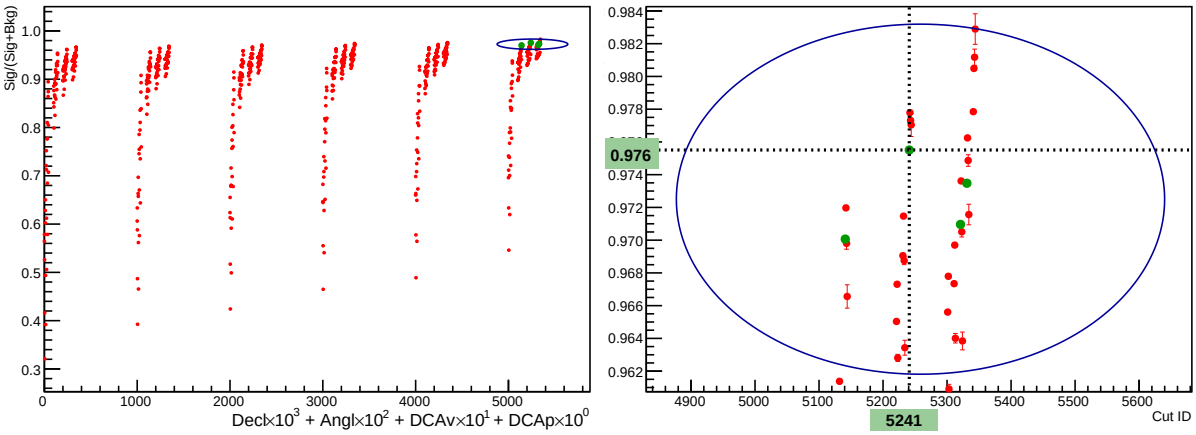

(b) K^0_S purities versus cut index

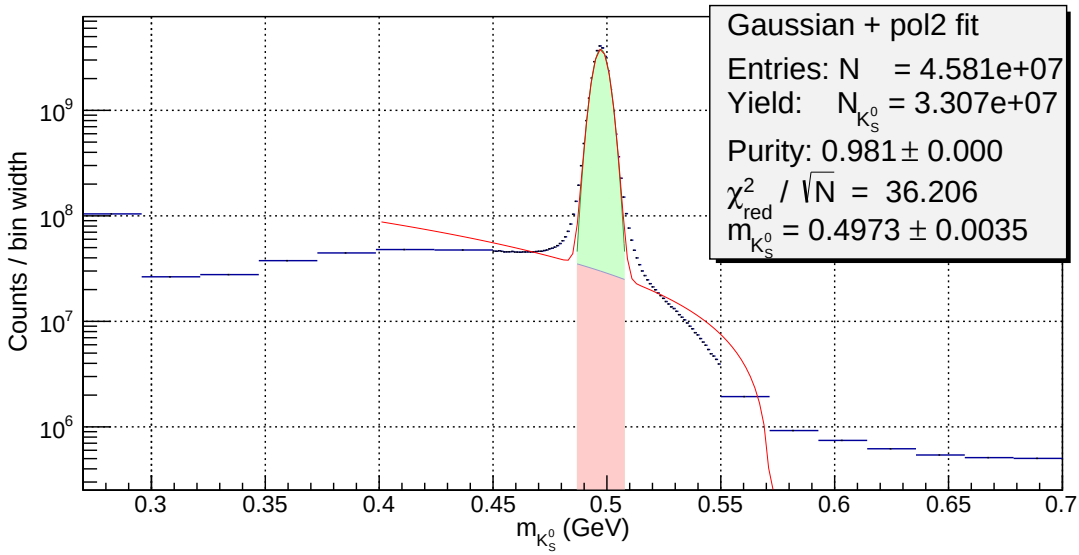

(c) Resulting invariant K^0_S mass distribution and fit (red). Only the shaded area is integrated over in the purity and yield computation. This is the distribution of the K^0_S candidates that were used in the correlation, not that of the systematic cut study, hence it displays a slightly different purity.

Figure 11: Finding the optimal cut index for high K^0_S yield and purity.

The purity and yield dependencies are presented in Figures 12a and 13a. The error bars in the purity graphs are defined as $1/\sqrt{\text{Sig+Bkg}}$. They are thus simple *statistical* error bars and that extend outside the maximal purity 1.
The background is stronger around 3 GeV/c, which can also be noticed in Figure 10. The fact that purity increases with increasing multiplicity bin is probably due to lower statistics and has no physical grounds.

The K^0_S purity dependence on p_T can be used to define *pair purity*, knowing the purity of the protons in the same p_T bin. Since the K^0_S purity is rather high, it has not been done in this study (see Section 5.3).

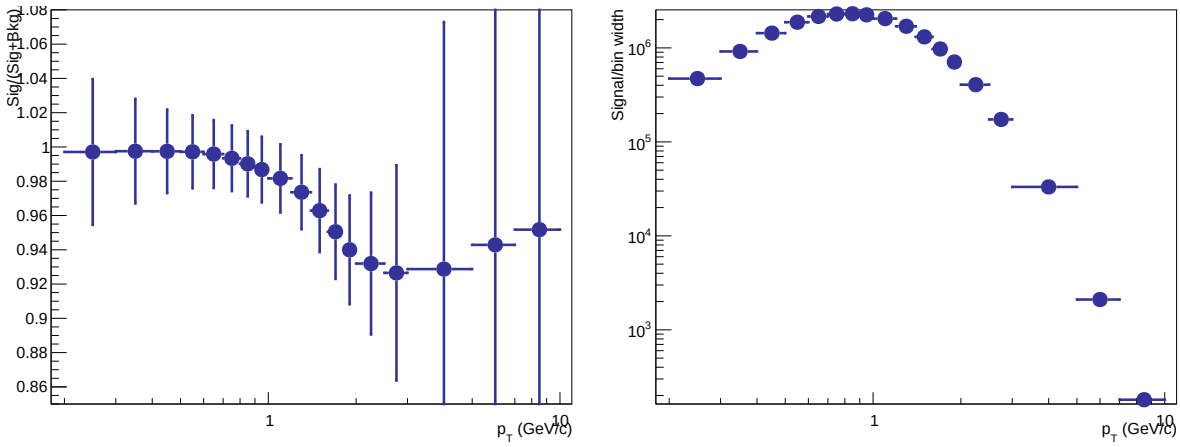

(a) K^0_S purity versus p_T

(b) K^0_S yield versus p_T

Figure 12: Purity and yield dependencies versus transverse momentum (p_T-axis in logarithmic scale).

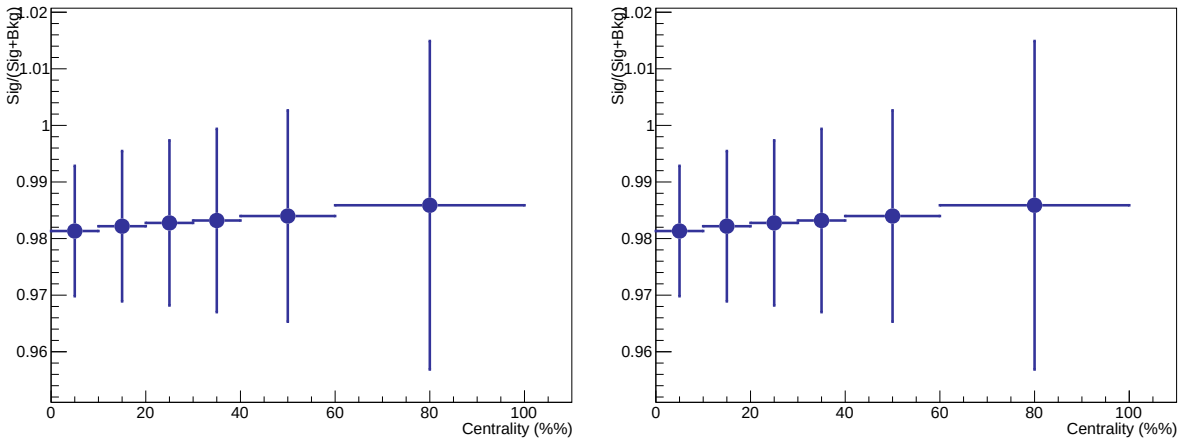

(a) K^0_S purity versus multiplicity bin

(b) K^0_S yield versus multiplicity bin

Figure 13: Purity and yield dependencies versus multiplicity bin.

4.1.1 Other possible K^0_S fits

The fit to the invariant K^0_S-mass distribution in Figure 11 is bad around the shoulders of the Gaussian. This could be due to ordinary background. To test this, different polynomial background fits have been tested in order to reproduce these shoulders while not letting the derivative of the polynomial become too large (that is, extrapolate the background in a continuous curve) and also fitting on different ranges (see Figure 14). Bad fits at the sides of the range have been ignored as they do not contribute to the purity and yield. The effect was that the purity and yield decreased, but that the shoulders could not be reproduced. The shoulders are most likely the result of reflections or secondaries, so this should be taken into account in the correlations.

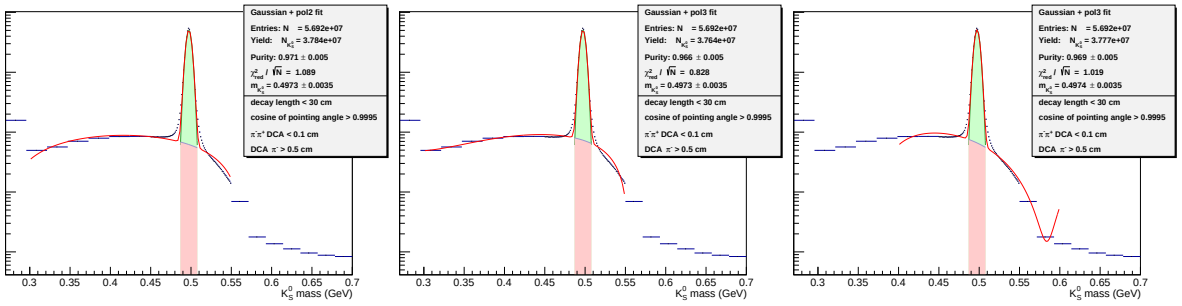

(a) Polynomial of degree 2, 0.3 to 0.55 GeV, purity 0.971

(b) Polynomial of degree 3, 0.3 to 0.55 GeV, purity 0.966

(c) Polynomial of degree 3, 0.4 to 0.6 GeV, purity 0.969

Figure 14: Comparison of different background fits for the invariant K^0_S mass distribution.

4.2 Proton purity weights

Since proton identification relies on nSigma cuts, it is reliable only up to around 3 GeV/c. The momentum dependence of the proton purity is due to the overlap of the $\frac{dE}{dx}$ distribution for protons with that of other particle species. Since higher p_T might be of interest too, an analysis of the proton purity and yield as a function of p_T has been performed. A total of 18 p_T bins with the following edges in GeV/c has been used in the analysis.

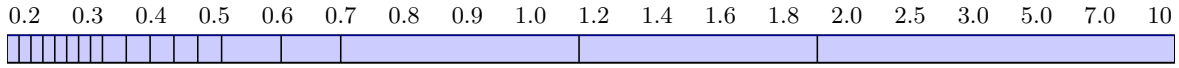

For each of these p_T bins, the purity and yield per particle was computed as described in Section 3.2. Purity below 0.2 GeV/c is taken to be that of the first bin, purity above 10 GeV/c that of the last bin. Since at high p_T the bins are wider, a logarithmic scale on p_T is used in the purity and yield graphs. For each of these p_T bins the proton purity was computed using the method described in Section 3.2.
Experimental distributions for each of the four particle species were obtained by selecting tracks with 0.5SigmaTOF. The total of these four distributions was fitted to an nSigmaPTPC distribution to which a less tight SigmaTOF cut had been applied. This was done for three different nSigmaTOF cuts in the proton hypothesis: 1, 2, and 3 SigmaTOF. The fits on the 1SigmaTOF cut are shown in Figure 15 and the fits on the 3SigmaTOF cut are shown in Figure 16. The data included in these distributions comes from all multiplicity bins. Note that this fit method can result in purities larger than 1, because the sum of the four particle distributions can be larger than that of the fitted black distribution.

Yields are defined as the integral over the scaled particle distribution over the full range (-24 to 25 SigmaTPC). The resulting particle yield graphs are shown in Figure 17. These yield graphs have been used to correct the fits. In some of the p_T bins (particularly above 2 GeV) some of the particle distributions were scaled too large or too small. This resulted in discontinuities in the yield graphs. A second fit was therefore applied over the scaled particle distributions with limits set on the four scale parameters in order to scale down the particle distribution to an expected yield. First, the electron distributions were rescaled, then the kaon yields, and finally the pion yields. The proton yields were not corrected.

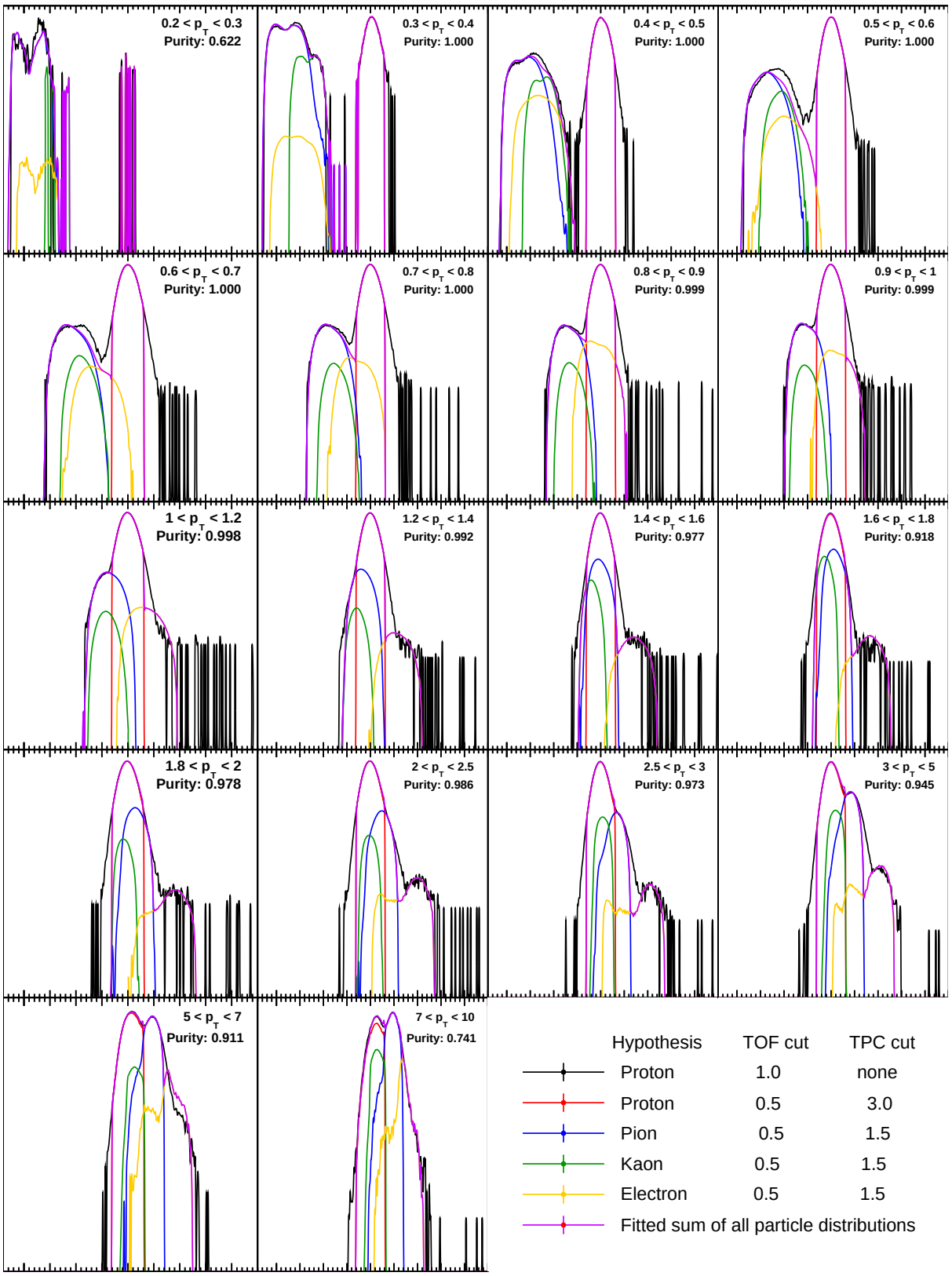

Figure 15: nSigmaTPC distributions fitted with particle distributions for **1SigmaTOF**. The x-axis ranges from -24 to 25 SigmaPTPC with the red proton distribution centered around 0. The black nSigmaPTPC distribution has been fitted by sum of the particle distributions (purple). The four scaled particle distributions (tight nSigma cuts) are explained in the legend.

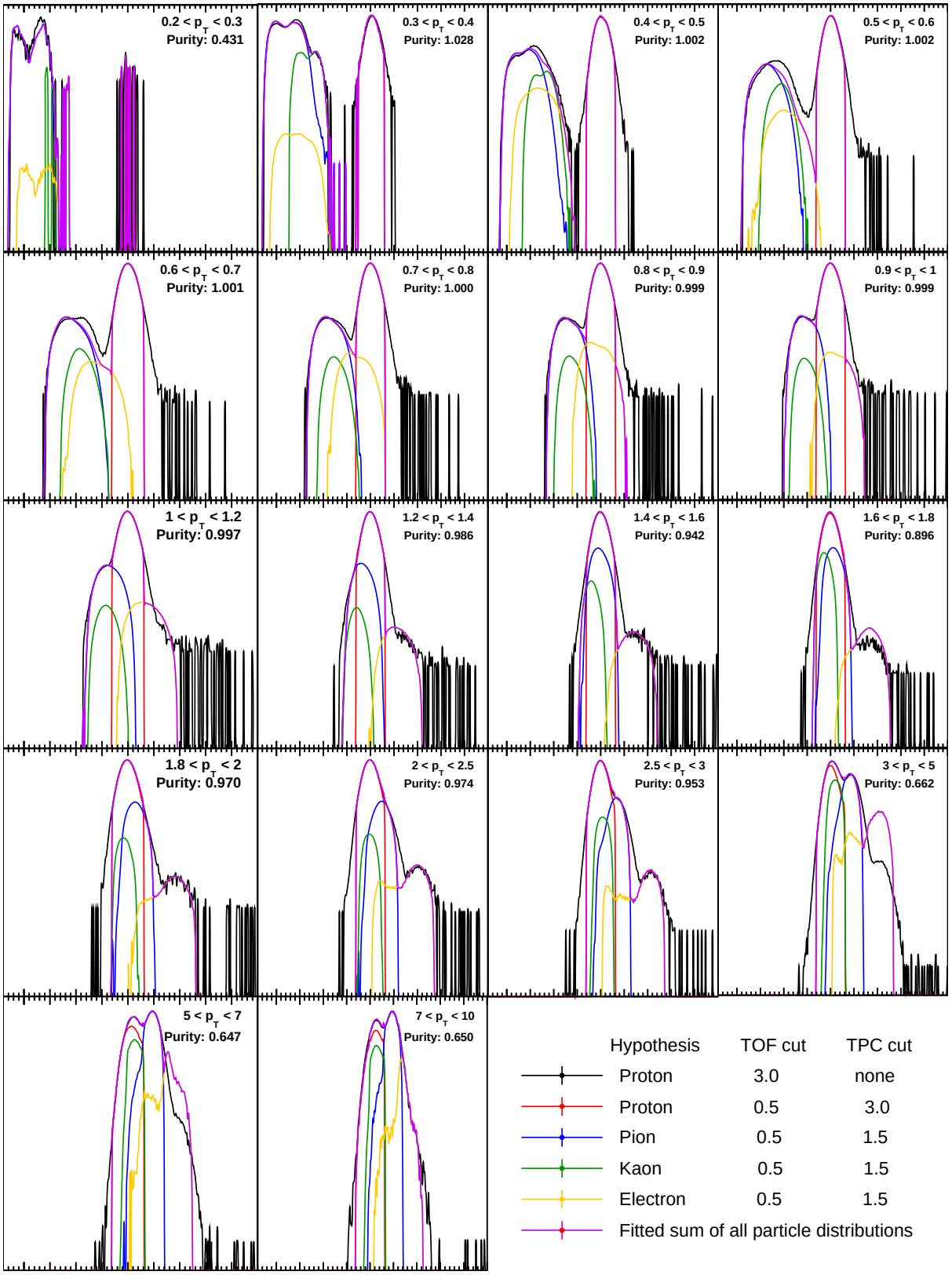

Figure 16: nSigmaTPC distributions fitted with particle distributions for **3SigmaTOF**. The x-axis ranges from -24 to 25 SigmaPTPC with the red proton distribution centered around 0. The black nSigmaPTPC distribution has been fitted by sum of the particle distributions (purple). The four scaled particle distributions (tight nSigma cuts) are explained in the legend.

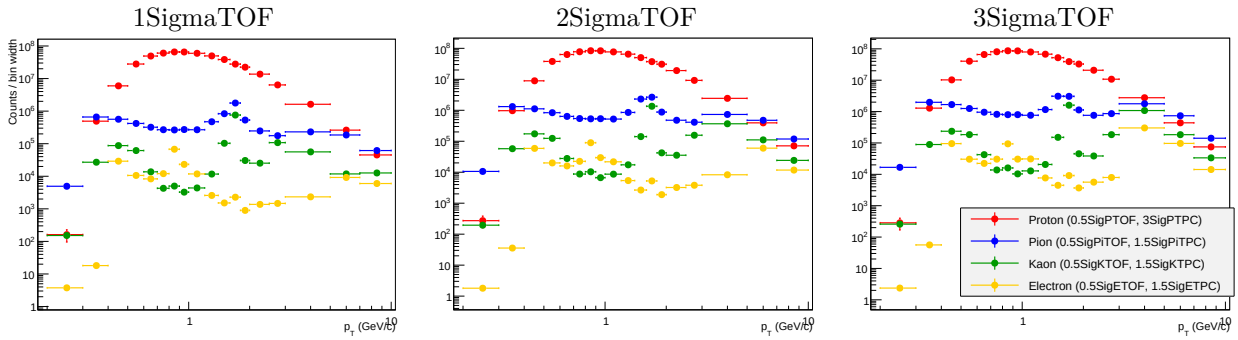

Figure 17: Scaled particle distribution yields for each of the three TOF cuts.
The legend in the right panel shows which cuts have been used for the four particle distributions.

The purity is computed from the fits. It is defined as the integral over the red proton distribution over the range -3 to 3 SigmaTPC (the 'signal') divided by that over the purple fitted sum (the 'background + signal'). The three resulting purity versus p_T-graphs (one for each TOF cut) are shown in Figure 18. Purities are high (nearly 1) up to about 2 GeV/c. This is because the proton β band by which the nSigmaPTOF is defined, is highly separated in this range, as can be seen more clearly in the 2-dimensional distribution in Figure 2a. The low purities in the first p_T bin is due to low statistics.
However, when simply looking at the fitted p_T-slices in Figures 15 and 16 the high purity is less clear. In the range up to 0.7 GeV/c, the sum of the particle distributions can be fitted quite exactly as the individual Gaussians can still be distinguished. The particle distributions other than protons fall outside the integral range. From around 0.7 GeV/c the electron distribution (yellow) starts to move to the same location as that of the proton (red). This is where the fit start to become unreliable. The fits start to become even less reliable around 1.2 GeV/c where the pion and kaon distributions move into the integration range. In these and in higher p_T bins, the yield graphs in Figure 17 have been used to rescale particle distribution that got too large yields. This was particularly necessary in the p_T range 1.4 to 3 GeV/ where the kaon (green) and/or pion (blue) distributions were centered around 0 and the black distribution had no shoulder to be fitted on.

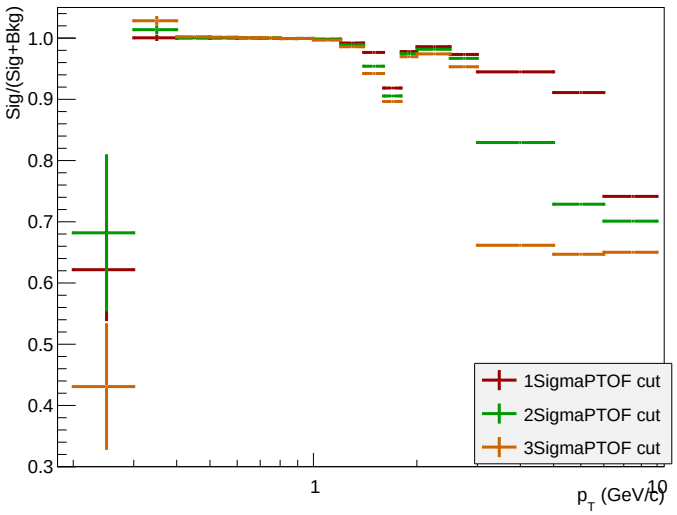

Figure 18: Purities for each of the three SigmaTOF cuts.

The resulting purity to p_T dependence is, even though it is based on these scaled and rescaled fits, like what we expect. The behaviour can be explained by looking at the $\frac{dE}{dx}$- and β-distributions in Figures 2b and 2a. For instance, the dip in purity around 2 GeV/c can be explained by the fact that the proton band in the $\frac{dE}{dx}$ distribution moves through the kaon and pion bands here. The decrease in purity from 4 GeV/c comes from the fact that the proton band in the *beta* distribution merges with the other bands from 4 GeV/c on.
Note that this fit method is based on the assumption that the particle distributions are nearly Gaussian and that only the particle of interest contributes to it. This is however clearly not the case in for instance the kaon and pion distributions at low p_T bins which show *two* Gaussian peaks. Furthermore, the distributions should show Gaussian behaviour at the sides, but they are cut of by their tight 1.5SigmaTPC cut. The purple sum thus does not fit well to the black distribution on certain nSigmaTPC ranges. This fact can be ignored however due to the fact that the purity is computed only in the range -3 to 3 nSigmaTPC.

4.3 K^0_S-p correlation

Protons have been correlated with K^0_S using different one-dimensional representations of their relative momentum (see Section 3.3.3). The correlation procedure produced foreground and combinatorial background distributions that were used to construct two correlation functions. Cuts used to select the two particles are given below.

Proton selection criteria	K^0_S selection criteria
$\|\text{nSigmaTPC}\| < 3$ and $\|\text{nSigmaTOF}\| < 1$	decay length < 30 cm
Number of clusters > 70	cosine of the pointing angle > 0.9995
Energy loss $\frac{dE}{dx} > 10$	DCA between the pions < 0.1 cm
$\chi_{\text{TPC}} < 3.5$	DCA of each pion > 0.5 cm
positive charge	

The resulting multiplicities of both particles per multiplicity bin are shown in Figure 19. For each K^0_S-p combination in an event and in the next events (event mixing), the three one-dimensional relative momentum representations q_{inv}, q, and q_{T} were calculated by the method explained in Section 3.3.3. This was done with weights and without weights. The resulting $3 \times 4 = 12$ distributions are presented in Figure 20. The distributions that used the same variable have been plotted together. The distributions with weights have been normalized to unity and the distributions without weights have been scaled down by the integral over the original weighted distributions. Errors are statistical (see Section 2.3) and are negligible small due to the high statistics (14.8M pairs). To make the small discrepancies between the distributions clearer, the distributions have been drawn like curves and their errors are not shown.

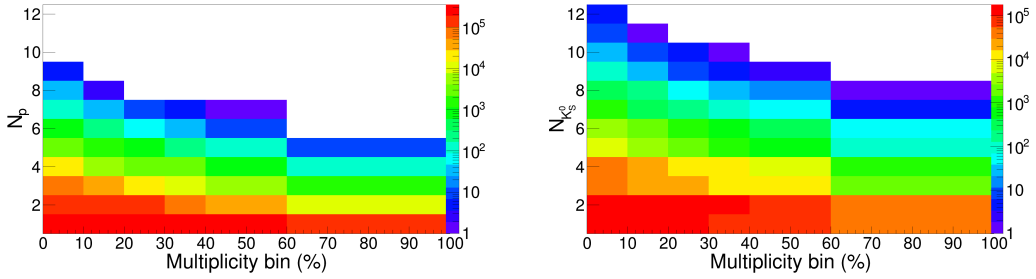

(a) Proton multiplicities (26.6M in total) (b) K^0_S multiplicities (35.1M in total)

Figure 19: Multiplicities per multiplicity bin of the two correlated particles.

Already from these distributions it can be seen that there is a discrepancy between the foreground and the background distributions. The fact that there is hardly any difference between the distributions with and without weights is due to the fact that most particles have a transverse momentum of around 1 GeV/c where the purity is largest, so few relative momenta of K^0_S-p combinations are computed with low weights. Besides that, since we are looking at the *relative* momentum, this small number of low-weight pairs is 'smeared out' over the correlation distribution.
For the correlation ratio function it is important to note that using q as a variable (Figure 21b) results in low statistics around 0 GeV/c. Statistics around 0 GeV/c are larger when using q_{inv} and q_{T}.

To analyze the difference in the foreground and background distributions, the correlation difference functions C_{dif}, as has been defined in Section 3.3.3, is presented in Figure 21. The figures present the correlation difference function of both weighted and none weighted distributions. In these graphs, error bars are computed using propagation of errors without covariance correction, where the errors used are the statistical errors of the correlation distributions mentioned before. Bin contents have been divided by the width of the p_{T} bins. The scale is small because all differences have been divided by the number of entries.
Figure 21 clearly shows that the correlation function is hardly any different when using weights. For this reason, the correlation without weights is not used and only the weighted distributions are used in what follows. It is also clear that there is a correlation between K^0_S and protons, since if there were no correlation, the data points would be lying on the green 0-line. As for the nature of this correlation,

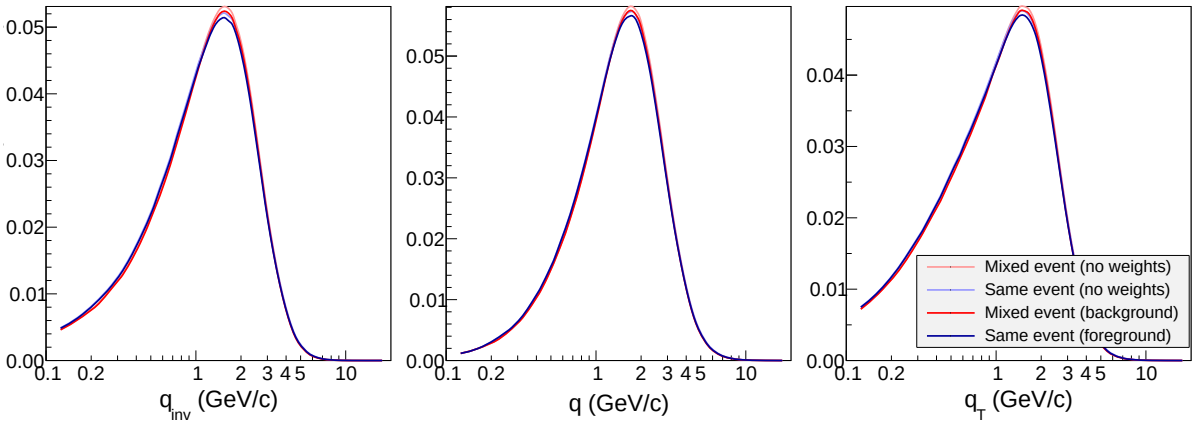

(a) q_{inv} distributions (b) q distributions (c) q_{T} distributions

Figure 20: Correlation distributions for different one-dimensional representations of relative momentum $\vec{q}$. The distributions without proton purity weights are also included, but can hardly be distinguished. A logarithmic scale has been used to enlarge the lower $\vec{q}$ range.

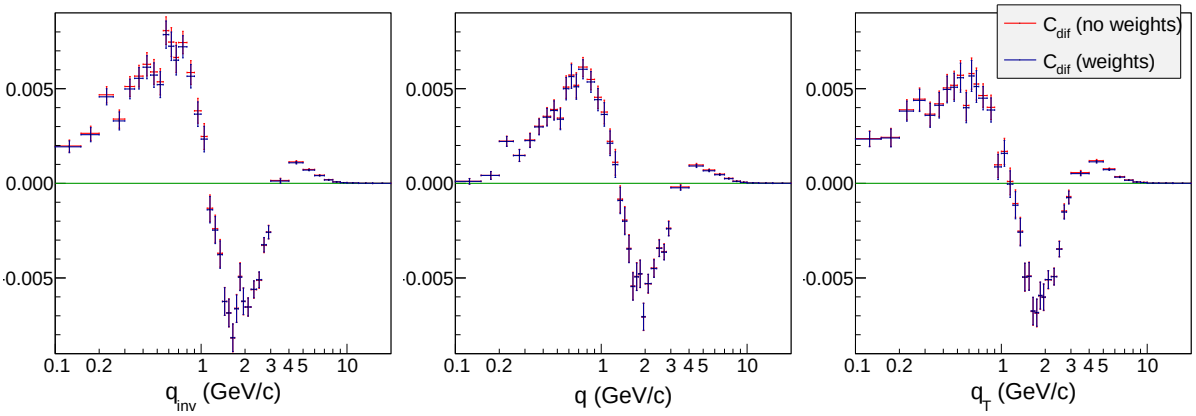

(a) $C_{\mathrm{dif}}\left(q_{\mathrm{inv}}\right)$ distributions (b) $C_{\mathrm{dif}}\left(q\right)$ distributions (c) $C_{\mathrm{dif}}\left(q_{\mathrm{T}}\right)$ distributions

Figure 21: Correlation difference function $C_{\mathrm{dif}}\left(K\right)$ for different one-dimensional representations of relative momentum K. The function computed without proton purity weights is also included. A logarithmic scale has been used to enlarge the lower K range where differences are strongest.

the correlation ratio function needs to be studied. As explained in the introduction, the ratio correlation function in particular can provide information of the space-time extend of the particle emitting region. Note also that multiplicity bins haven't been used so far. The distributions above were computed over all multiplicity bins. The study of the correlation ratio function will be performed in multiplicity bins as experience shows that correlation behaviour is different in different multiplicity bins.
Figure 22 shows the correlation ratio functions C_{rat} in the six multiplicity bins as a function of the three variables q_{inv}, q and q_{T}. The errors are again computed using error propagation without covariance correction. For each multiplicity bin and each variable, a Gaussian function

$$C(K) = \lambda \exp\left(K^2/2\sigma^2\right) + 1 \tag{10}$$

has been fitted to the graph in the range $0 < K < 1.6$ GeV/c. As can be seen in the figures, above this maximal K value the correlation ratio function becomes less than 1 (it 'dips' below 1) and the Gaussian cannot be fitted properly.[14] The fit parameters and χ^2_{red} are shown in each multiplicity bin panel.

[14] The K value where the correlation ratio function dives below 1 is different for each variable and each multiplicity bin, but the value 1.6 GeV/c is found to match most of the graphs.

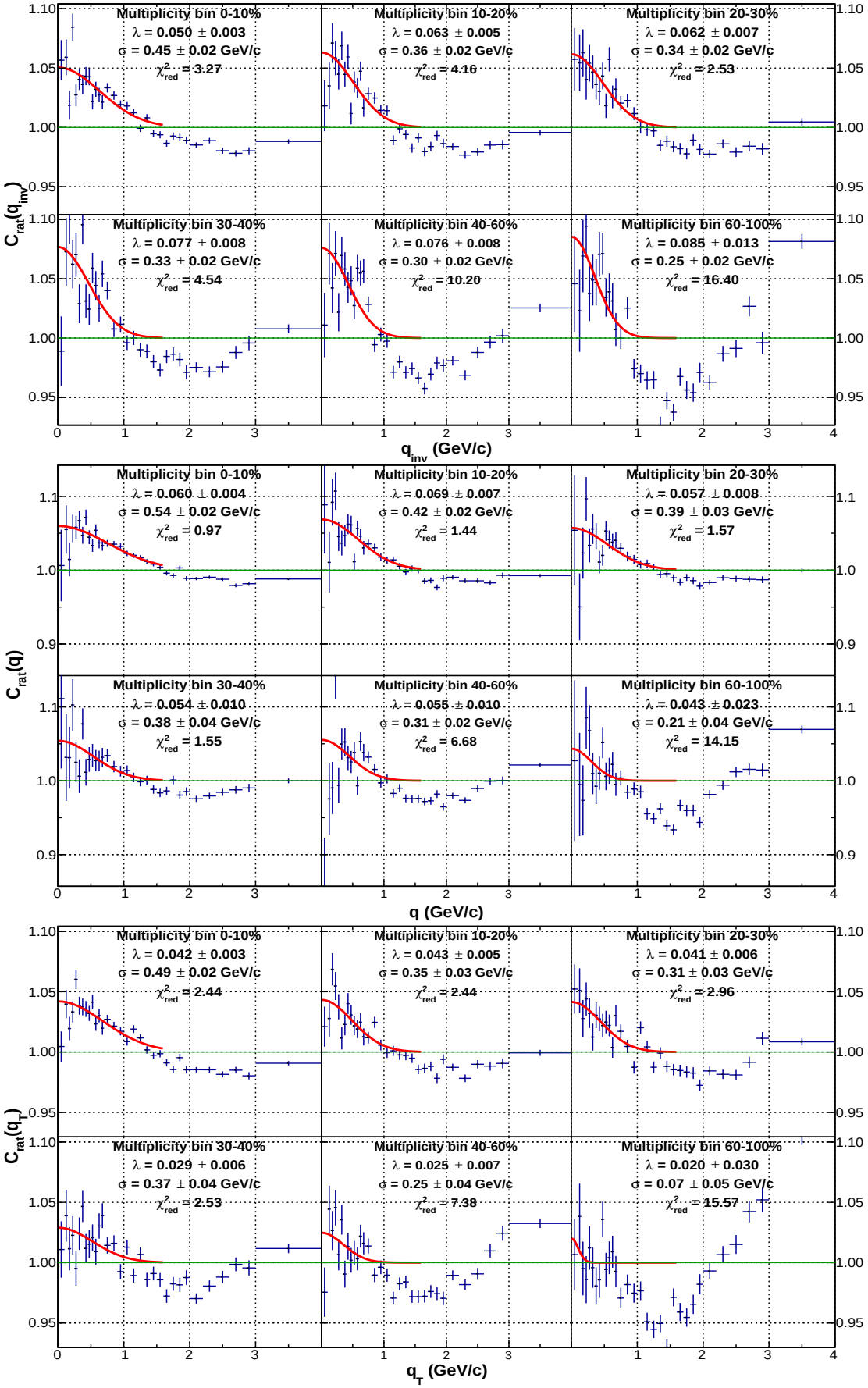

Figure 22: Correlation ratio function $C_{\mathrm{rat}}(K)$ in the range $0 < p_{\mathrm{T}} < 4$ GeV/c.

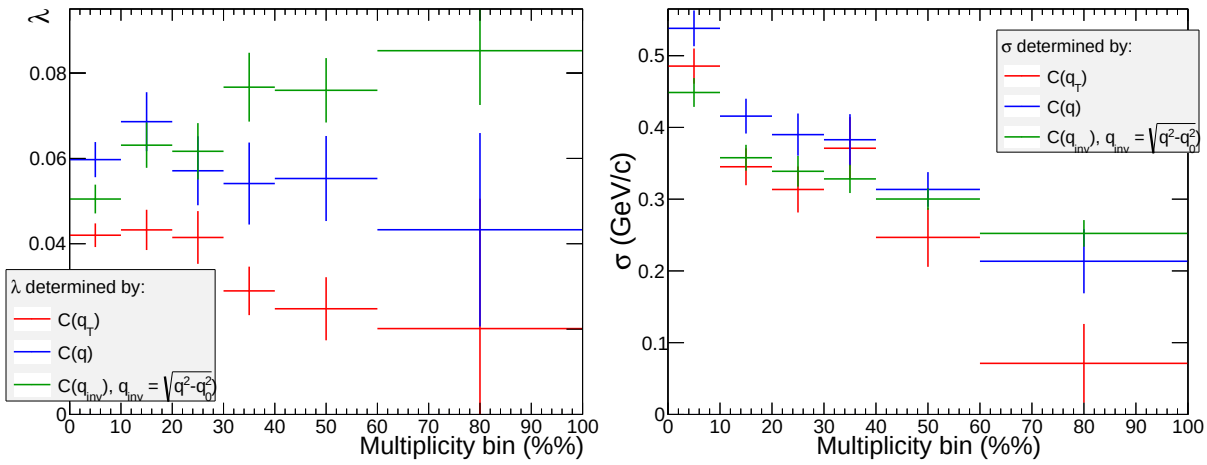

(a) Height parameter λ

(b) Width parameter σ

Figure 23: The two Gaussian fit parameters versus multiplicity bin for each variable q_{inv}, q, and q_{T}.

The fits in Figure 22 show that q_{inv} can be used better as a variable for the correlation ratio function. The behaviour of C_{rat} with the non-relativistic variables q and q_{T} is 'less Gaussian' around 0 GeV/c than that of the relativistic variable q_{inv}. The difference is particularly clear in high multiplicity bins, even though error bars are large in these bins. The difference can be explained by the fact that most emitted particles in ALICE travel with relativistic velocities (see Figure 2b). This indicates that the relativistic variable q_{inv} is more reliable.

Interestingly, the fit parameters λ and σ as a function of multiplicity bin (see Figure 23) show comparable behaviour when using the non-relativistic variables. The fact that using q_{T} results in smaller λ and σ, that is, a smaller and less Gaussian peak, indicates that the correlation function is weakened, meaning that the z-component which is included in q, should not be ignored at these energies.

More remarkable is the fact that λ increases in higher multiplicity bins when using q_{inv}, but decreases when using the non-relativistic variables. This fact is hard to explain, but it indicates again that it is important to use relativistic variables at high collision energies. The parameter σ for q_{inv} shows behaviour similar to that of the non-relativistic variables, depends less strongly on multiplicity.

Thus far, only low relative momenta have been analyzed. As noted before, the correlation ratio function dives below 1 from around 1.6 GeV/c to around 3.5 GeV/c. This effect is due to the fact that the foreground and background distributions are normalized to each other, so that the weighted integral of the ratio of both distributions should be 1. However, from around $q_{\text{inv}} \approx 3.5$ GeV/c, the correlation ratio function increases rapidly, as can be seen in Figure 24.[15] The effect is less strong at low multiplicity bins (high multiplicity). This is also where the statistics start to decrease, as can be seen in Figures 20. The fact that the effect is stronger at peripheral collisions (high multiplicity bins) could indicate that it is caused by low statistics. The increase of the correlation ratio function, as opposed to its decrease around 2 GeV/c, has not been noticed in similar studies, see Section 5.1.

[15] Only q_{inv} is shown, because q_{T} and q show similar behaviour.

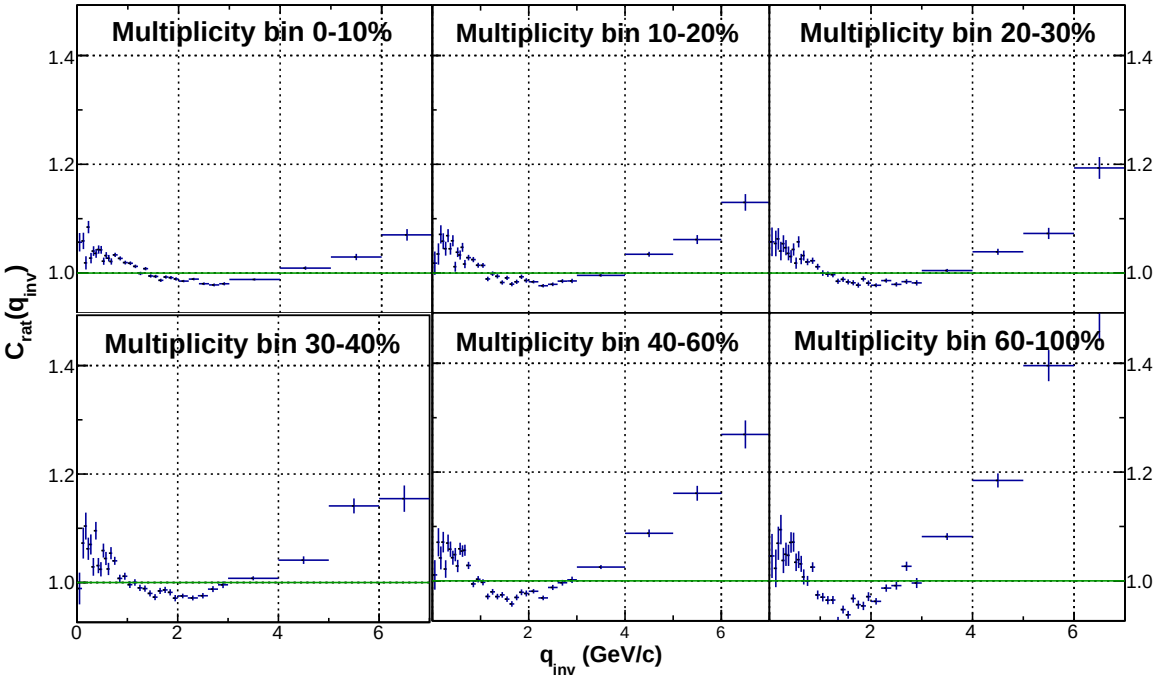

Figure 24: Correlation ratio function $C_{\mathrm{rat}}(q_{\mathrm{inv}})$ for high q_{T}.

5 Discussion and conclusion

This study of $\mathrm{K}^0_{\mathrm{S}}$-p correlations in p-Pb collisions has been exploratory, as correlations between these particles at these energies have not yet been studied. The results have therefore been presented without thorough conclusions. This section first compares the correlation results with that of another study at lower energies in the Alternating Gradient Synchrotron (AGS) located at the Brookhaven National Laboratory. A comparison is then made with a different particle correlation in the same data set: $\mathrm{K}^0_{\mathrm{S}}$-$\mathrm{K}^+$ correlation. The result of this second correlation study indicates that further study is required. Therefore the experience gained in this study is elaborated in the last subsection and is concluded with a hypothesis and with suggestions for further analysis.

5.1 Comparison with correlation results from AGS

The E895 Collaboration has investigated a number of mixed-particle correlations in 2, 4, 6, and 8 A GeV/c Au-Au collisions at the AGS.[12] The study focussed on correlations with the Λ-hyperon, but also included an analysis of $\mathrm{K}^0_{\mathrm{S}}$-p correlation. The reconstruction of Λ (decay mode $\mathrm{p}+\pi^-$, branching ratio 64%) and of $\mathrm{K}^0_{\mathrm{S}}$ was done in a similar way as in this paper using the invariant mass distribution of the Λ and $\mathrm{K}^0_{\mathrm{S}}$ candidates.

Four momentum correlations were studied: p-Λ, p-$\mathrm{K}^0_{\mathrm{S}}$, π^--Λ, and π^--$\mathrm{K}^0_{\mathrm{S}}$. As in this study, the correlation ratio function C_{rat} was used (named C in the AGS paper), but here the non-relativistic variable q was used (K is used instead of q). The correlation ratio function was fitted with the Gaussian function given in Equation (6). The results are shown in Figure 25. The group found that p-Λ shows correlation, but that p-$\mathrm{K}^0_{\mathrm{S}}$, π^--Λ, and π^--$\mathrm{K}^0_{\mathrm{S}}$ do not. Figure 25b shows that these distributions are essentially flat at 6 GeV. These correlations were therefore not interpreted by the group.

The momentum range is also of a much different scale: the correlation function was studied only up to 0.1 GeV/c. At higher K, the correlation function converged to 1. The p-Λ distribution was fitted with the Gaussian function for different energies, see Figure 25a. The resulting σ were consistent in the different collision energies and were around $\sigma = 27$ MeV. The p-Λ results were interpreted by using simulations that were designed to simulate collisions with correlation. The simulation codes needed a Gaussian source of radius R_g and a scattering length as input. The scattering length is a known theoretical quantity, while

R_g gives an estimate of the extend of the particle emitting region. R_g determines the width σ of the distribution. The width σ thus gives an indication of the extend of the particle emitting region.

The fact that K^0_S-p did not show any correlation at all as opposed to the K^0_S-p correlation in this study, may be due to the fact that the scattering length of K^0_S-p is very small, but it could also come from the fact that much lower energies are used at AGS. However, other studies, such as source [11] where K^0_S-K^0_S correlation was analyzed in Pb-Pb collisions in ALICE, show similar σ-widths as that in the AGS paper. The width σ of the fitted Gaussian in this study is larger by a factor one hundred, indicating that another physical mechanism might cause the K^0_S-p correlation.

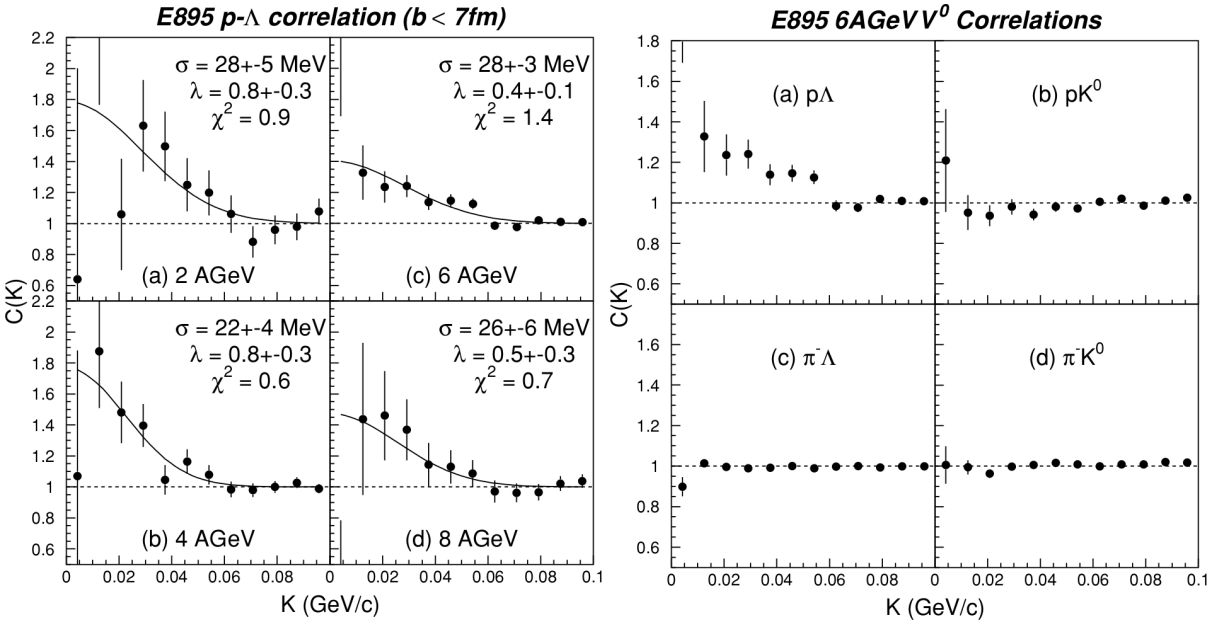

(a) p-Λ correlation at semi-centrality in p-p collisions for different collision energies. The correlation ratio function has been fitted with a Gaussian function as in Equation (10).

(b) Different particle correlations at 6 GeV at AGS. These panels show that p-K^0_S, π^--Λ and π^--K^0_S correlations are essentially flat at these energies as opposed to p-Λ correlation.

Figure 25: Correlation results from the E895 collaboration in p-p collisions at the AGS. The definition of K is that of q in this paper and the definition of $C(K)$ is that of $C_{\text{rat}}(q)$. See source [12].

5.2 Comparison with K^0_S-K^+ correlation

As a final check, K^0_S has also been correlated with K^+ to verify if the correlation ratio function displays similar σ-widths. The K^0_S-K^+ correlation was done in exactly the same manner as the K^0_S-p correlation except that K^+ were selected using the following cuts.

- $\sqrt{(n\sigma_{\text{TPC}})^2 + (n\sigma_{\text{TOF}})^2} < 2$
- Number of clusters > 70
- $\chi_{\text{TPC}} < 3.5$
- Energy loss $\frac{dE}{dx} > 10$
- Positive charge

This resulted in a total of 41.2M kaons and 23.8M pairs. No weights were used in this correlation analysis. Note that a 'radial' nSigma cut has been used, cutting TOF and TPC at once. The results of the correlation are shown in Figure 26. Only the relativistic q_{inv} variable has been used, because it proved to be the most reliable (Section 4.3), but the λ and σ dependence on multiplicity has been computed for the three variables.

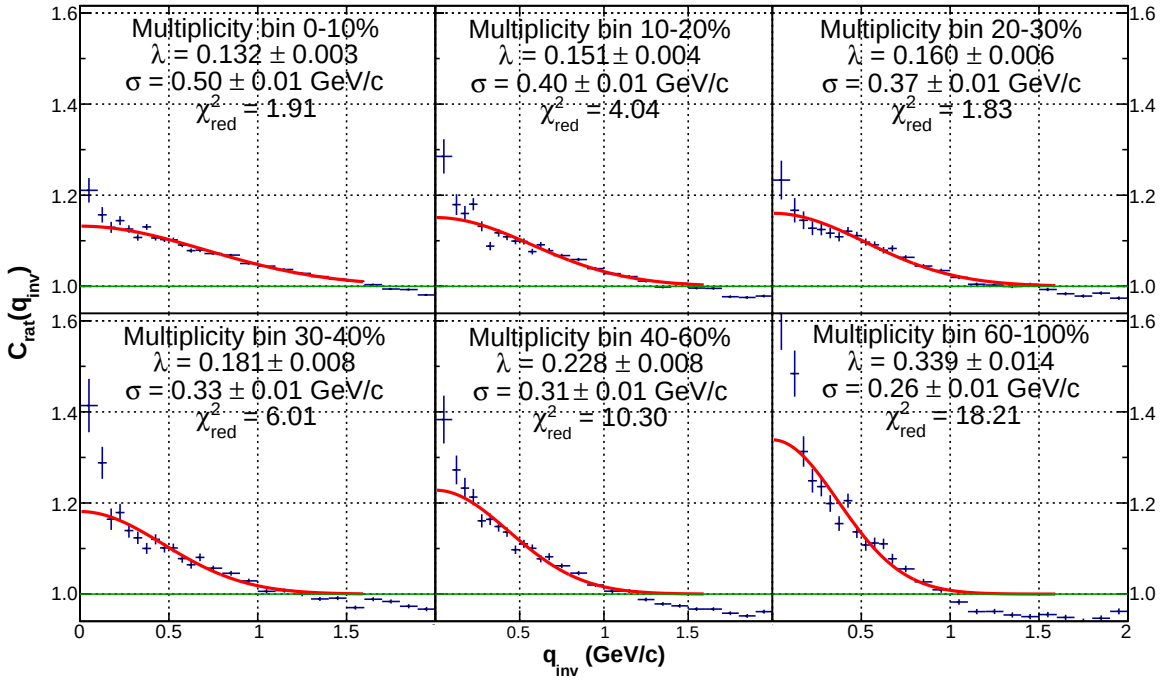

(a) Low $q_{\rm inv}$ with fitted Gaussian of Equation (10).
A detailed $q_{\rm inv}$ scale has been used to enlarge the second Gaussian near 0 GeV/c.

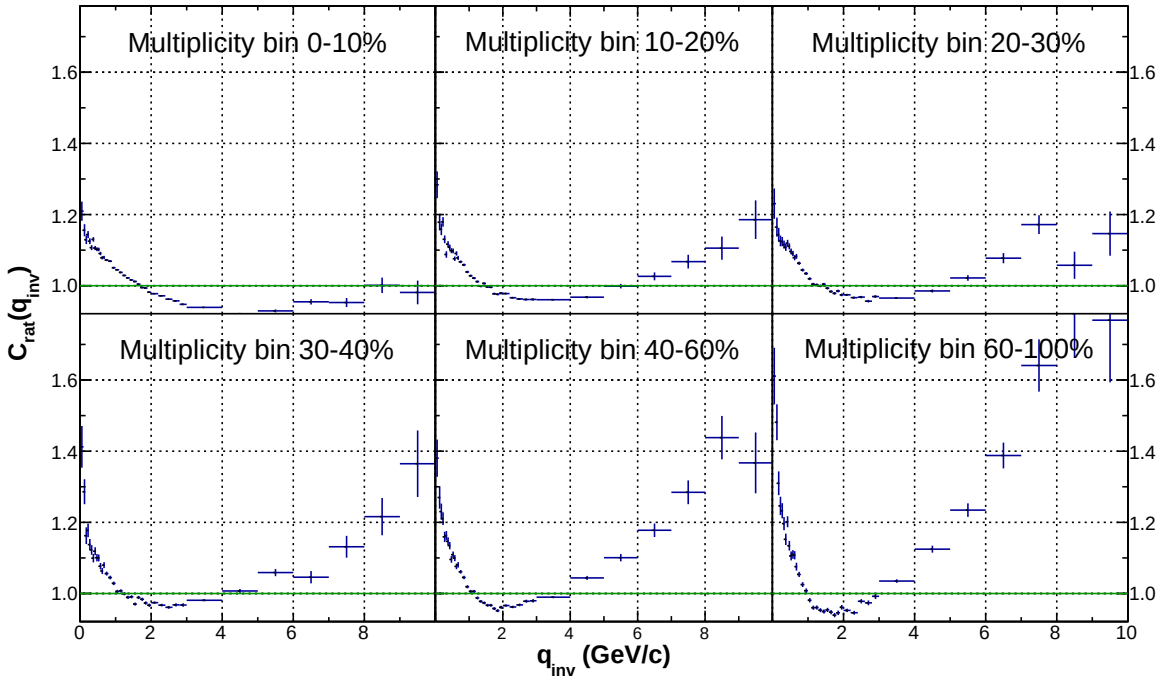

(b) The high $q_{\rm inv}$ range shows the same rising behaviour as in K^0_S-p correlation.

Figure 26: The correlation ratio function $C_{\rm rat}(q_{\rm inv})$ for K^0_S-K^+ correlation in different multiplicity bins.

The correlation graphs in Figure 26 have some remarkable features. At first sight, the behaviour is much the same as that of K^0_S-p in Figure 22 and 24, but a closer look reveals a smaller correlation signal around 0 GeV/c that could be due to the $K^+ + K^- \rightarrow K^0 + K^0$ decay channel. It is however remarkable that the width of this 'second Gaussian' is in the order of that in the AGS paper. Small statistics in this low q_{inv} range however, prohibit quantitative analysis.

On the other hand, the behaviour at high q_{inv} is indeed the same as in K^0_S-p correlations, as can be seen in Figure 26b. The 'larger' Gaussian behaviour around 0 GeV/c, has been analyzed by fitting. The fit parameters versus multiplicity bin in Figure 27 show that this behaviour is in the same order of magnitude as that K^0_S-p correlation in Figure 23. The λ parameter however increases when using both the non-relativistic and relativistic variables. The σ behaviour is the same as that of Figure 5.3.

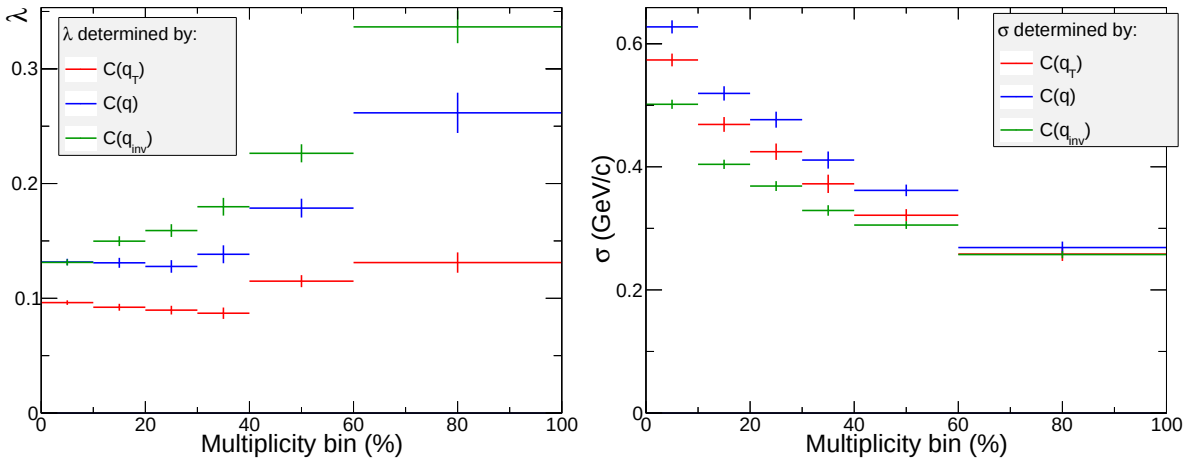

(a) Height parameter λ

(b) Width parameter σ

Figure 27: The two fit parameters versus multiplicity bin for each variable in K^0_S-K^+ correlation.

5.3 Conclusion and suggestions

This study was an introductory study in K^0_S-p correlations in p-Pb collisions in ALICE. Findings are therefore summarized below and suggestions for further research are given afterwards.

Conclusions and findings

- K^0_S can be reconstructed with large yields and high purity. Purity decreases around momenta of 3 GeV/c and increases with higher multiplicity bins.
- Extracting the purity as a function of transverse momentum by scaling experimental particle nSigmaTPC distributions proves to be a reliable method. Purity decreases from around 4 GeV/c and there is a dip around 2 GeV/c. Using proton purity as weights has a negligible effect on the correlation function.
- There is a non-negligible discrepancy in foreground and background distribution when correlating K^0_S with protons. The correlation difference function can give insight in the magnitude of this discrepancy and the correlation ratio function C_{dif} provides information of the physical processes that lie behind the discrepancy.
- Using the relativistic one-dimensional representation q_{inv} of the relative momentum proves to be a more reliable variable in the correlation function. The fit parameter λ *increases* with higher multiplicity bins when using q_{inv}, while λ *decreases* when using the non-relativistic variables q and q_{T}. Using q_{T} results in smaller and less strong Gaussian peaks in the correlation ratio function.

- At high relative momentum, the correlation ratio function rises sharply. The effect becomes stronger in high multiplicity bins. This effect is hard to explain, but also arises in K^0_S-K^+ correlation at these high collision energies.

- A dip in the correlation ratio function is present around 2 GeV/c. This comes as a 'compensation' to the higher values outside this range. Other studies, like source [14] and [4], also notice this effect, although the effect in these studies is smaller when comparing it to the Gaussian peak than is the case in this study.

- Correlating K^0_S with K^+ reveals 'double' correlation behaviour. On top of the strong correlation behaviour discussed below, a small peak is revealed around 0 GeV/c. This could be due to K^0_S-K^+ correlation within the particle emitting region.

- The ratio correlation function shows a strong correlation effect in both K^0_S-p and K^0_S-K^+ correlation. Gaussians fit to this correlation function in the range 0 to 1.6 GeV/c show that the width of these correlation peaks are too wide to come from . The effect can be explained by the presence of *particle 'mini-jets'*.[14] A parton emitted from the primary vertex decays into a jet of particles that move into the same direction. Protons and K^0_S in such a jet thus have a small relative angular momentum and contribute to a peak in the correlation ratio function. However, the behaviour in this study (the peak around 1 GeV/c, the dip around 2 GeV/c, and the rise at high relative momenta) is much stronger than that in other studies, which raises doubts about this 'mini-jet' hypothesis.

Suggestions for further study
The 'mini-jet effect' needs further study. One has to find a way to remove this background effect. Here are three suggestions that could be useful for further studies.

- In some studies, *pair purity* is used in the correlation. It is defined as the product of the two particles in their respective momentum bins. This can be done for K^0_S and protons as well, although the fact that the K^0_S purity is larger than 0.9 in all p_T bins indicates that the effect will probably be small.

- In many studies, such as [11] and [14], correlation is studied in k bins, where k is the sum of the momenta of the two correlated particles (see Figure 9). These studies often find that correlation is more distinguishable in low k bins. It could also be of help in removing the jet-like background, since particles coming from these jets often have high momenta.

- Although simulating p-Pb collisions is difficult (see Section 2.2), developing a simulation for this type of collisions can be used to prove the 'mini-jet' hypothesis, as was done in source [12].

References

[1] ALICE: Physics Performance Report, Volume I,
Journal of Physics G: Nuclear and Particle Physics, Vol. 30, No. 11 (2004)

[2] U.A. Wiedemann, U. Heinz, Phys. Rept. 319, 145 (1999)

[3] Lisa, Pratt, Soltz, Wiedemann, "Femtoscopy in Relativistic Heavy Ion Collisions: two decades of progress", 5 Sep. 2005

[4] S. Bekele, R. Lednický, "Neutral kaon correlations in $\sqrt{S_{NN}} = 200$ GeV Au+Au collisions at RHIC". *Brazilian Journal of Physics, vol. 37, no. 3A, Sep. 2007*

[5] "$K^0_S K^0_S$ correlations in pp collisions at $\sqrt{s} = 7$ TeV from the LHC ALICE experiment", 10 Jun. 2012, arXiv:1206.2056v1 [hep-ex]

[6] "Long-range angular correlations of π, K and p in p-Pb collisions at $\sqrt{s_{NN}} = 5.02$ TeV.", 16 Oct. 2013 arXiv:1307.3237v3 [nucl-ex]

[7] S. Eidelman et al (2004). "Review of Particle Physics 2004 – Strange Mesons". *Particle Data Group.* `http://pdg.lbl.gov/2004/listings/s012.pdf`

[8] J. Beringer et al. (2012): "Particle listings – K0. *Particle Data Group.* `http://pdg.lbl.gov/2012/listings/rpp2012-list-K-zero.pdf`

[9] E.M. Henley, A. Garcia, "Subatomic Physics", 3rd edition, 2007.

[10] Dhevan Gangadharan, "Two and Three-Pion Quantum Statistics Correlations in Pb-Pb Collisions $\sqrt{s_{NN}} = 2.76$ TeV at the LHC", 16 Sep. 2013.

[11] Matthew Steinpreis, Ohio State University,
"Neutral kaon femtoscopy in PbPb collisions at $\sqrt{s_{NN}} = 2.76$ TeV",
16 Oct. 2012

[12] "Neutral strange particle dynamics in Au+Au collisions at AGS energies",
2002 J. Phys. G: Nucl. Part. Phys. 28 1567
`http://iopscience.iop.org/0954-3899/28/7/307`

[13] S. Bekele, "Charged and neutral kaon correlations in Au–Au collisions at $\sqrt{s_{NN}} = 200$ GeV",
2004 J. Phys. G: Nucl. Part. Phys. 30 S229

[14] "Femtoscopy of pp collisions at $\sqrt{S_{NN}} = 0.9$ and 7 TeV at the LHC with two-pion Bose-Einstein correlations.", 19 Jan. 2011
arXiv:1101.3665v1 [hep-ex]